Journal of Structural Dynamics, 3, (pp. 58-87) 2025
Understanding Limitations of Nonlinear Damping Ratio Identification Methods from Force Appropriation Tests

Understanding Limitations of Nonlinear Damping Ratio Identification Methods from Force Appropriation Tests

Benjamin R Pacini [*1], Robert J Kuether [†1], and Deborah M Fowler [‡1]

[1] *Sandia National Laboratories, P.O. Box 5800 – MS0557, Albuquerque, NM 87185*

Abstract

Energy dissipation (i.e., damping) is a critical quantity to identify in order to understand the dynamic performance of a mechanical design as the dissipation directly influences response amplification near resonance. In linear systems, dissipation is often modeled with constant viscous damping for each mode and can be extracted directly from modal tests in the form of damping ratio. For nonlinear systems there have been many proposed techniques for characterizing damping from experimental measurements, however researchers have yet to reach a consensus on a unified approach. This work investigates three damping identification methods and evaluates each of their limitations. The context for the identification is the nonlinear force appropriation testing technique. The study conducts virtual experiments utilizing multi-harmonic balance solutions where phase resonance is enforced on single-degree-of-freedom models with different nonlinearities – both conservative and non-conservative. In this way, the calculated damping ratios are compared directly to corresponding analytical approximations from the models to enable a critical assessment of their accuracy and of any limitations of each damping identification technique. Additionally, the effect of higher harmonics (both in phase resonance and uncontrolled) on the damping ratio estimates is explored by including an electro-mechanical model of a shaker. In addition to identifying limitations for each damping identification technique considered, this work shows that the trend in the damping ratio does not necessarily reflect the true nature of the nonlinear damping restoring force. Moreover, the damping ratio trend identified from nonlinear force appropriation experiments is sensitive to higher harmonics in the excitation force regardless of whether they are maintained in phase resonance or uncontrolled.

Keywords: Nonlinear damping identification; phase resonance testing; nonlinear structural dynamics

Received on October 8, 2024, *Accepted on February 26, 2025*, *Published on March 14, 2025*

1 Introduction

In the design of structures subject to vibration, margin to failure is directly related to the amplitude of response. One of the key factors that contribute to response amplitude is damping. Thus, much effort is expended to determine the damping associated with each mode of vibration. A typical industrial practice is to identify damping from an experiment and use these empirical values with a correlated finite element model (FEM). This FEM can then be used to evaluate the design to relevant inputs, conduct parametric studies, and many other tasks pertinent to ensuring the structure achieves the desired performance in service. The relevance of these evaluations depends on the accuracy of the damping identified from experiment, so it is essential that this quantity be accurately characterized.

For linear structures, damping is typically extracted from linear curve fits of frequency response functions (FRFs) measured during a modal test conducted either with hammer taps or shaker excitation and is quantified via the

[*] brpacin@sandia.gov
[†] rjkueth@sandia.gov
[‡] dfowler@sandia.gov

damping ratio [1, 2]. For nonlinear structures, the experiments and identification techniques to identify damping is an open area of research [3, 4] and many methods have been proposed and developed, as reviewed in [5]. One class of methods rely on ring-down data measured from experiments to identify the amplitude-dependent damping ratio backbone curve – a review of methods applied specifically to jointed structures can be found in [6]. For example, the methods in [7, 8, 9] utilize the Hilbert transform to extract the damping ratio curves from freely decaying responses. Other methods use forced response from electrodynamic shakers, such as the method in [10], which determines stiffness and damping by curve fitting quasi-linear representations of each mode to the restoring force. Damping of nonlinear structures can also be characterized from stepped sine excitation, for example, parametrically [11] and non-parametrically [12]. These represent a few of the many widely available strategies that have been developed over the last several decades.

The present work focuses on nonlinear modal methods using nonlinear force appropriation (NFA) testing to isolate the primary resonance of the structure. The objective is to isolate a single nonlinear normal mode (NNM) of interest using modal shaker excitation with a sinusoidal force and adjust the excitation frequency until phase resonance is achieved. There are two approaches to NFA testing discussed in the literature. The first approach is to turn off the shaker once phase resonance is achieved and measure the freely decaying response and estimate the frequency and damping ratio backbone curve using methods discussed earlier [13, 14]. The second approach, and the one that is used throughout this study, is to repeat the phase resonance excitation for sequentially increasing input levels so that the nonlinearity is characterized from low to high-level response amplitudes [15, 16]. This can be readily achieved with closed-loop controllers such as Phase-Locked-Loop [16, 17] or control-based continuation [18]. Measurements from these experiments typically include excitation force and dynamic response (e.g., acceleration) as well as the fundamental frequency at each input level where phase resonance was achieved. In this work, only primary phase resonances are considered [19, 20] where 90 degrees relative phase (i.e., phase quadrature) is achieved between the excitation force and acceleration response at the same frequency (whether the fundamental or integer harmonics of the excitation frequency). Cenedese and Haller [21] showed the conditions in which the conservative NNMs can be excited in the forced and damped case, leading to further justification of the use of force appropriation to measure the nonlinear modes of structures with arbitrary damping sources.

Extracting the amplitude-dependent natural frequencies and deflection shapes from the NFA experiments is straightforward, as the fundamental frequency corresponds to the excitation frequency once phase quadrature is achieved and the shapes at resonance are measured with the deployed sensing strategy. However, the damping ratio backbone curve requires further post-processing and is an indirect quantity that must be computed from data. There are relatively few papers that directly discuss the extraction of the damping ratio curve from NFA tests. One such paper is presented by Scheel et al. in [15] which relies on the Extended Periodic Motion Concept (EPMC) [22]. The approach is rooted in the energy balance method, where at resonance, the input energy from the external excitation is balanced by the dissipated energy, providing a direct relation between the damping and input force. This has been demonstrated in the context of nonlinear modal analysis in [23, 24, 21, 25]. Other methods rely on the relationship between the measured hysteresis curves of an oscillator over a cycle of vibration and the corresponding energy dissipated. While conducted outside the context of NFA testing, several papers have demonstrated this relationship in the case of frictionally damped systems, where the hysteresis loop in the modal domain can be used to extract the amplitude-dependent damping ratio curve [8, 26]. Another approach to estimate damping is based on a linearization of the FRF where the amplitude dependent modal properties can be identified. An example of this method applied to stepped-sine testing can be found in [27] where the amplitude-dependent damping is extracted from multiple response levels.

The objective of this work is to evaluate and explore the limitations of the different damping ratio identification techniques that utilize measurements from a NFA test. This study conducts virtual NFA experiments on three nonlinear single degree-of-freedom (SDOF) oscillators using phase-resonance multi-harmonic balance (PR-MHB) with constraints to enforce phase between excitation force and drive-point response [28]. This essentially simulates the phase resonance nonlinear modes (PRNMs) of the system [20]. The outputs of PR-MHB algorithm are the same as those produced by NFA experiments and are thus amenable to the damping ratio identification techniques considered in this work. Additionally, the PR-MHB technique can incorporate an electromechanical model of a modal shaker [29] to investigate the influences of shaker-structure interactions, which can be significant in the identification process [30]. The three nonlinear SDOF systems considered are a Duffing oscillator (i.e., cubic stiffness), an oscillator with a contact-gap type stiffness nonlinearity, and an oscillator with a Jenkins element to simulate friction [31, 32]. These were selected since they each represent different nonlinear physics that are typically observed in experiments with mechanical systems, so the performance of each damping ratio identification technique for these physics can be examined. Using this approach, the identified damping ratios from the different NFA methods can be compared to analytical approximations.

The contributions of this work include the comparison and evaluation of the limitations of three nonlinear damping ratio identification techniques, which utilize data from NFA experiments. First order approximations of the solutions to the equations of motion for each nonlinear oscillator are also provided to corroborate the numerical results. Further, second order approximations are derived to demonstrate the influence of controlled (i.e., maintained in phase resonance) and uncontrolled (i.e., resulting from shaker-structure interactions) higher forcing harmonics on the identified damping ratio results. All these results provide evidence of the limitations of the damping ratio backbone curve identified from NFA experiments.

The remainder of this article is outlined as follows. Section 2 provides a background on PRNMs as well as the PR-MHB techniques utilized in this work. The three nonlinear damping ratio identification techniques are introduced and evaluated in a single-harmonic excitation context in Section 3 and align closely with those described above. The first technique considered was that developed by Scheel et. al. [15] mentioned previously. The second utilizes the hysteresis loop of the damping force in modal space to extract the amplitude-dependent damping ratio. The last technique considered assumes a linearized response at each excitation level achieved in the NFA and solves for the associated damping ratio via the linear FRF equation. Section 4 describes the three nonlinear SDOF systems considered as well as select MHB results, including the damping ratios identified using the three techniques from Section 3. The damping ratio results are validated in Section 5 using first order approximations of the solutions to the equations of motion of the three nonlinear SDOF systems. The effects of controlled and uncontrolled higher forcing harmonics are explored in Section 6. Conclusions are presented in Section 7.

2 Phase Resonance Background

The intent of the damping identification techniques is to estimate amplitude-dependent damping ratio curves from measurements taken during force appropriation tests. This work focuses on the use of simulated force appropriation data using MHB [28] to solve the equations of motion for various nonlinear SDOF systems. This is achieved by simulating the harmonically forced response with additional constraints to enforce phase resonance between the excitation and response at specified harmonics included in the Fourier basis. Note that forcing is only applied to the fundamental frequency and its integer harmonics since these analyses are limited to periodic motions. The details of the algorithm are found in [28], which effectively computes the phase resonant modes for the primary resonances of the structure [20, 19]. The equation of motion for a nonlinear, SDOF system is given as

$$m\ddot{x} + c\dot{x} + kx + f_{nl}(x, \dot{x}) = f \tag{1}$$

where m, c, and k are the mass, linear viscous damping, and linear stiffness, respectively. The nonlinear force, f_{nl}, is a function of the displacement, x, and velocity, $\dot{x}$, and the excitation force is given as f. Note the time dependence of x, $\dot{x}$, $\ddot{x}$, and f have been excluded for clarity. MHB is used to solve Equation 1 with x and f written as finite Fourier series which is a summation of N_h harmonic signals:

$$x(t) = \frac{X_{0,c}}{\sqrt{2}} + \sum_{n=1}^{N_h} X_{n,c} \cos n\omega t + X_{n,s} \sin n\omega t \tag{2}$$

$$f(t) = \frac{F_{0,c}}{\sqrt{2}} + \sum_{n=1}^{N_h} F_{n,c} \cos n\omega t + F_{n,s} \sin n\omega t \tag{3}$$

A constraint is added to the MHB solver to enforce 90 degrees phase lag between the excitation force and the displacement at the fundamental frequency and any specified harmonics, achieving the primary phase resonance [20, 19, 28]. Note that in this work, primary phase resonance refers to satisfying this phase quadrature condition between the excitation force and displacement at the same harmonic index, not just the fundamental. Therefore, only those harmonics that are selected to be in phase resonance will have non-zero forcing Fourier coefficients in Equation 3; all other forcing Fourier coefficients are enforced to be zero.

The phase resonance constraints are applied in the following manner. Equations 2 and 3 are inserted into Equation 1 and the harmonics are balanced. This creates $2N_h + 1$ equations with $4N_h + 2$ unknowns which are the Fourier Coefficients of the displacement and force as well as the fundamental frequency ω. For each harmonic index n selected to be in phase resonance, the general phase lag constraint can be written as:

$$-\tan^{-1}\left(\frac{F_{n,s}}{F_{n,c}}\right) + \tan^{-1}\left(\frac{X_{n,s}}{X_{n,c}}\right) - \frac{\pi}{2} = 0 \tag{4}$$

Monophase motion is also assumed, so, to avoid potential of discontinuities resulting from the use of $\tan^{-1}$, the constraint defined by Eq. 4 is enforced numerically by constraining $F_{n,c} = X_{n,s} = 0$ for the harmonics selected to be in phase resonance. Additionally, both forcing Fourier Coefficients are set to zero for harmonics not selected to be in phase resonance. These $2N_h$ constraints supplement the $2N_h + 1$ equations of motion, resulting in a system that is uniquely solvable. Pseudo-arc length continuation [33] is used to solve the system of equations, resulting in the fundamental frequency ω and the Fourier Coefficients of displacement and force for each solution step.

The MHB approach taken here to solve the nonlinear equations of motion is consistent with force appropriation testing [13]. Typical force appropriation tests utilize single point excitation and achieve local phase resonance, the same conditions in the MHB simulation. While there are many outputs available from MHB, only those that are readily measurable during a force appropriation experiment are used in the damping ratio identification techniques. These quantities are the excitation frequency as well as the Fourier Coefficients for each harmonic of the excitation force and displacement response. While displacement is not a typical measurement available for structural dynamics testing, converting between acceleration and displacement is trivial for signals that are multi-harmonic sinusoids. Additionally, the modal properties of the underlying linear system are assumed known as these can be extracted from traditional modal testing.

One major difference between simulated experiments using MHB as formulated above and force appropriation testing is that shaker-structure interactions present in the latter can produce harmonics in the measured excitation force that are not present in the former [30]. Therefore, Section 6 uses a modified MHB algorithm that includes an electromechanical model of a modal shaker [29] in order to study the effect of shaker-structure interactions on, and any corresponding limitations of, the identified damping ratio. In this framework, the input is no longer excitation force, but rather the voltage output from the data acquisition system (DAS). The excitation force into the structure under test (the nonlinear SDOF oscillators) becomes a function of the responses. Constraints from Equation 4 can therefore still be applied to maintain phase resonance at the fundamental frequency, which are enforced on the internal reaction force between the shaker and structure under test, rather than the externally applied forces. In this case, the sine and cosine magnitudes of the input voltages are adjusted until the monophase internal forces are in phase quadrature with the corresponding response harmonics.

3 Nonlinear Damping Ratio Identification Techniques

This work evaluates three different techniques to extract damping ratio from data typically available from a nonlinear force appropriation experiment. These techniques assume that the mode of interest is sufficiently isolated in phase resonance (either through force appropriation in test or with constraints in MHB as described in Section 2 in numerical studies) and that all other modes are negligibly excited. Additionally, no internal resonances are activated. The first two approaches utilize work-energy relationships (Sections 3.1 and 3.2) whereas the last treats each response where phase resonance is achieved as a linearized response and thus employs the linear FRF equation (Section 3.3). Section 3.4 compares the techniques and identifies limitations associated with the practical implementation of each.

3.1 Damping Ratio Under the Extended Periodic Motion Concept Framework

The first technique for extracting damping ratio from a force appropriation test was taken from Scheel et al. [15]. A brief overview will be given here. It was derived from the EPMC where the multi-DOF nonlinear equations of motion are written as:

$$\mathbf{M}\ddot{\boldsymbol{x}} + \mathbf{K}\boldsymbol{x} + \boldsymbol{g}(\boldsymbol{x}, \dot{\boldsymbol{x}}) - \xi\mathbf{M}\dot{\boldsymbol{x}} = \mathbf{0} \tag{5}$$

where $\mathbf{M}$ and $\mathbf{K}$ are the linear mass and stiffness matrices, respectively, $\boldsymbol{g}(\boldsymbol{x}, \dot{\boldsymbol{x}})$ is a vector of additional linear damping forces and the nonlinear forces, and ξ is called the self-excitation factor. The $-\xi\mathbf{M}\dot{\boldsymbol{x}}$ term is used to force the equation to be periodic and, at resonance, balances the energy dissipated by the damping forces in $\boldsymbol{g}(\boldsymbol{x}, \dot{\boldsymbol{x}})$ over a period of vibration.

The forcing term $-\xi\mathbf{M}\dot{\boldsymbol{x}}$ is an idealized multi-DOF, multi-harmonic force. In [15], this is approximated by a single input that is in phase quadrature with the drive point response at the fundamental frequency. When the primary resonance has been achieved, the appropriated forcing vector is:

$$\boldsymbol{f}^{\boldsymbol{appr}} = \boldsymbol{u} f^{appr} \approx \xi\mathbf{M}\dot{\boldsymbol{x}} \tag{6}$$

where the superscript “appr” indicates the conditions where the appropriated force has been achieved and the $\boldsymbol{u}$ is a unit vector with a 1 at the drive point DOF.

To derive the amplitude-dependent damping ratio, [15] introduces the active power P defined in [16] as:

$$P = \frac{1}{T}\int_0^T \dot{x}_{dp}^{appr} f^{appr} dt \tag{7}$$

where $\dot{x}_{dp}^{appr}$ is the drive point velocity, f^{appr} is the excitation force, and T is the period of the fundamental excitation frequency ω. Note that in general, x_{dp} and f are multi-tone signals. When the forcing is correctly appropriated, and recognizing that ξ is the same for all harmonics, Equation 6 can be used with Equation 7 to compute ξ using the fundamental component of the active power, P_1:

$$\xi = \frac{2P_1}{\omega^2 \boldsymbol{\psi}_\mathbf{1}^{\boldsymbol{H}} \mathbf{M} \boldsymbol{\psi}_\mathbf{1}} \tag{8}$$

where $\boldsymbol{\psi}_\mathbf{1}$ is the complex operational deflection shape of the fundamental displacement response. The damping ratio is computed as

$$\zeta_{EPMC} = \frac{\xi}{2\omega} \tag{9}$$

This value is computed for each solution found by MHB (or each excitation level where the primary resonance is achieved during a force appropriation test) using the force and response data. Repeating this for many different solutions (excitation levels), the amplitude-dependent damping ratio for a mode of interest can be obtained.

Note that from Equation 8 the mass matrix is required for this process. When applied to a finite element model, this is available. However, for an experiment, [15] proposes using the following:

$$\mathbf{M} \approx \left(\mathbf{\Phi}^{\mathbf{T}}\right)^{+} \mathbf{\Phi}^{+} \tag{10}$$

where $\mathbf{\Phi}$ is the mass-normalized mode shape matrix and the $+$ superscript refers to the generalized inverse. Additionally, this formulation for damping ratio allows for mode shapes to change since the deflection shape can be written as a mass normalized mode shape, $\boldsymbol{\phi}_1$, scaled by modal amplitude q: $\boldsymbol{\psi}_1 = q\boldsymbol{\phi}_1$. Thus, $\boldsymbol{\psi}_1^H \mathbf{M} \boldsymbol{\psi}_1 = q^2 \boldsymbol{\phi}_1^H \mathbf{M} \boldsymbol{\phi}_1 = q^2$. Because only one mode is considered, any change in shape is accounted for by the modal scaling q, guaranteeing that a $\boldsymbol{\phi}_1$ can be found that satisfies $\boldsymbol{\phi}_1^H \mathbf{M} \boldsymbol{\phi}_1 = 1$.

3.2 Damping Ratio from Modal Power

The second technique is based on the modal formulation of a nonlinear structure and utilizes the work done by the modal damping restoring force over a cycle of oscillation similar to [34] to compute damping ratio. During the force appropriation test, primary phase resonance is achieved for a single drive point. Assuming the response is dominated by a single mode k, the equation of motion is approximated as SDOF of the form [35]:

$$\ddot{q}_k + f_{d,qk}(q_k, \dot{q}_k) + f_{s,qk}(q_k, \dot{q}_k) = f_{qk} \tag{11}$$

where q_k is the modal displacement of mode k and is related to the physical response via the linear mode shape matrix:

$$\boldsymbol{x} = \mathbf{\Phi}\boldsymbol{q} \tag{12}$$

$$\boldsymbol{q} = \mathbf{\Phi}^{+}\boldsymbol{x} \tag{13}$$

with

$$q_k = \boldsymbol{u}_k \boldsymbol{q} \tag{14}$$

where u_k is the k^{th} unit vector. The terms $f_{d,qk}(q_k, \dot{q}_k)$ and $f_{s,qk}(q_k, \dot{q}_k)$ are the damping and stiffness restoring forces for mode k, respectively, that comprise both the linear and nonlinear terms. The modal force is f_{qk} and is related to the physical excitation force by

$$\boldsymbol{f_q} = \mathbf{\Phi}^T \boldsymbol{f} \tag{15}$$

and

$$f_{qk} = \boldsymbol{u}_k \boldsymbol{f}_{\boldsymbol{q}} \tag{16}$$

From Equations 14 and 16, if the primary phase resonance was achieved at the drive point, then it is reasonable to assume that the relative phase between q_k^{appr} and f_{qk}^{appr} is 90 degrees as well. Using the principles from [13] and [36], once the primary resonance has been achieved, the inertial and stiffness terms in Equation 11 sum to zero and are orthogonal to the damping and excitation force. Therefore,

$$\ddot{q}_k^{appr} + f_{s,qk}\left(q_k^{appr}, \dot{q}_k^{appr}\right) = 0 \tag{17}$$

and thus the damping forces are balanced by the excitation force:

$$f_{d,qk}\left(q_k^{appr}, \dot{q}_k^{appr}\right) = f_{qk}^{appr} \tag{18}$$

To compute the nonlinear damping ratio, the work done by $f_{d,qk}\left(q_k^{appr}, \dot{q}_k^{appr}\right)$ is computed using the area integral [37]:

$$W_{d,qk} = \oint f_{d,qk}\left(q_k^{appr}, \dot{q}_k^{appr}\right) dq \tag{19}$$

A linearized approximation of the damping force is used for each excitation level:

$$f_{d,qk}\left(q_k^{appr}, \dot{q}_k^{appr}\right) = 2\zeta\omega\dot{q}_k^{appr} \tag{20}$$

Recognizing $dq = \dot{q}dt$ and combining Equations 18 through 20 gives:

$$W_{d,qk} = \int_0^T 2\zeta\omega\dot{q}_k^{appr^2} dt = \int_0^T f_{qk}^{appr}\dot{q}_k^{appr} dt \tag{21}$$

Thus, the damping ratio for a given excitation level for a system at a primary phase resonance under the modal framework is:

$$\zeta = \frac{\int_0^T f_{qk}^{appr}\dot{q}_k^{appr} dt}{2\omega\int_0^T \left(\dot{q}_k^{appr}\right)^2 dt} \tag{22}$$

The appropriated modal force and corresponding modal velocity response are defined as follows:

$$f_{qk}^{appr}(t) = \sum_{n=1}^{N_h} F_{q,n,c}^k \cos n\omega t + F_{q,n,s}^k \sin n\omega t \tag{23}$$

$$\dot{q}_k^{appr}(t) = \sum_{n=1}^{N_h} V_{n,c}^k \cos n\omega t + V_{n,s}^k \sin n\omega t \tag{24}$$

The force in Equation 23 is written as multi-tone, but the only non-zero Fourier Coefficients are those associated with the harmonics chosen to be in phase resonance in the MHB computations. Inserting Equations 23 and 24 into Equation 22 and reducing to the only the fundamental component gives:

$$\zeta_q = \frac{F_{q,1,c}^k V_{1,c}^k + F_{q,1,s}^k V_{1,s}^k}{2\omega\left(\left(V_{1,c}^k\right)^2 + \left(V_{1,s}^k\right)^2\right)} \tag{25}$$

The general procedure for utilizing Equation 25 to extract the nonlinear damping ratio from an experiment or MHB results is to use Equations 13 and 15 to extract the modal velocity $\left(\dot{q}_k^{appr}\right)$ and force $\left(f_{qk}^{appr}\right)$ for mode k. Note that in practice, acceleration is typically the quantity measured, so the conversion from acceleration to velocity occurs either before or after the modal filtering process (i.e., the application of Equations 13). The frequency ω is assumed to be a known parameter (in force appropriation tests it is a controlled parameter and in MHB it is typically the continuation

parameter), so the Fourier Coefficients of $\dot{q}_k^{appr}$ and f_{qk}^{appr} can be extracted for each excitation level. These can then be used in Equation 25 to compute the amplitude-dependent damping ratio.

This process relies on the linear mode shape matrix $\mathbf{\Phi}$ as a modal filter to transform from physical to modal coordinates. It assumes that the mode shapes do not change with amplitude which is a limitation of this method. Weakly nonlinear systems tend to satisfy this condition of constant mode shapes, but this must be evaluated by the practitioner if this is appropriate for their particular case. Additionally, this method delineated the stiffness and damping forces into two separate terms $f_{d,qk}(q_k, \dot{q}_k)$ and $f_{s,qk}(q_k, \dot{q}_k)$. The damping identification technique presented in this section is still valid even if the restoring forces are not readily and explicitly separable into damping and stiffness portions (e.g., the Jenkins element presented in Section 4.3) since, at phase resonance, the harmonic representation of the restoring force will separate into two orthogonal Fourier Series where one is in phase with acceleration ($f_{s,qk}$) and the other in phase with the excitation force ($f_{d,qk}$)[36].

3.3 Damping Ratio from Linear FRF

The last technique explored in this work to extract damping ratio from force appropriation tests utilizes a linear FRF framework. The system is linearized at each excitation level such that the linear FRF equation is applicable. Assuming that the influence from other modes is negligible, i.e. the modes are well-spaced, the drive point accelerance FRF for mode k is:

$$H_{dp,k}(\omega) = \frac{A_{dp}(\omega)}{F(\omega)} = \frac{-\omega^2 \phi_{dp,k}^2}{\omega_{n,k}^2 - \omega^2 + i2\zeta_k \omega_{n,k}\omega} \tag{26}$$

where the subscript dp indicates drive point, so $\phi_{dp,k}$ is the linear, mass-normalized drive point mode shape value for mode k. Note that $\omega_{n,k}$ is amplitude-dependent resonant frequency for mode k but is assumed constant for a given amplitude. When the primary phase resonance is achieved, $\omega = \omega_n$ so that:

$$H_{dp,k}(\omega) = \frac{-\phi_{dp,k}^2}{i2\zeta_k} \tag{27}$$

Therefore, the nonlinear damping ratio under the linearized FRF framework can be computed at each excitation level as:

$$\zeta_H = \frac{\phi_{dp,k}^2}{2|H_{dp,k}(\omega)|} \tag{28}$$

where the subscript on the damping ratio has been updated to indicate the method used for its computation. Since the FRF in Equation 27 is evaluated at the fundamental frequency, $|H_{dp,k}(\omega)|$ is computed using the fundamental Fourier Coefficients of the drive point acceleration ($A_{1,c}$ and $A_{1,s}$) and excitation force:

$$|H_{dp,k}(\omega)| = \sqrt{\frac{A_{1,c}^2 + A_{1,s}^2}{F_{1,c}^2 + F_{1,s}^2}} \tag{29}$$

This formulation utilizes an accelerance FRF. Other FRFs can be used, but Equations 28 and 29 would need to be adjusted accordingly. Additionally, this method need not be restricted to using a drive point FRF, so long as accurate measures of the mass-normalized mode shape values for the excitation and response locations are used. In this case, $\phi_{dp,k}^2$ in Equation 28 would be replaced with $\phi_{i,k}\phi_{o,k}$ where the i and o indices correspond to the input and response locations, respectively. Lastly, this method assumes that the mode shapes are constant. Therefore, this method is restricted to cases where the mode shape does not change with amplitude.

3.4 Comparison of Techniques

Equations 9, 25, and 28 provide the three techniques for computing nonlinear damping ratio using data from force appropriation tests or simulations. EPMC was derived for multi-DOF systems, but Eq. 9 can be simplified if, as in this work, assuming an SDOF system:

$$\zeta_{EPMC} = \frac{F_{1,c}X_{1,s} - X_{1,c}F_{1,s}}{2m\omega^2\left(X_{1,c}^2 + X_{1,s}^2\right)} \tag{30}$$

While the following still holds true for multi-DOF systems, this SDOF formulation of ζ_{EPMC} makes it more readily apparent that the three damping formulations provide identical results under the following conditions:

1. Mode shapes are mass normalized and do not change with amplitude.
2. The target mode dominates the response with other elastic and rigid body modes providing minimal distortion.
3. Single input forcing (i.e., single input location/direction)

Note that SDOF was not a condition for similtude. However, even under these three conditions, there are certain limitations in their practical implementation that dictate when to use one damping ratio identification method over the other. Two of the three methods (EPMC and modal power) rely heavily on a well-defined mode shape matrix; it is used in EPMC to compute the experimental mass and the modal power method uses the linear mode shape matrix as a modal filter to transform from physical to modal coordinates. Therefore, these two methods are limited to cases where there is sufficient instrumentation freedom such that all modes within the bandwidth of interest are independently observable. Conversely, ζ_H relies only on the drive point shape and FRF, so only one response and one input force measurements are required. If EPMC or modal power methods were utilized in this manner with knowledge of only one input-output pair, large errors would result in the identified damping ratio due to, respectively, an inaccurate representation of the experimental mass $\mathbf{M}$ (see Eq. 10) and inadequate modal filter. Thus, if all the above conditions are met, ζ_H is the simplest method that will give the same results as the two, more complicated algorithms.

If there is evidence that the mode shapes are changing, ζ_{EPMC} is the recommended technique as it is the only one that allows for mode shape changes [15] while the other two are limited to cases where constant mode shapes. If the mode shapes are constant, ζ_q can filter out the response associated with rigid body modes (if applicable), which in certain circumstances can distort the drive point phase [38] (note that this would be a violation of condition 2 above). However, to fully realize this advantage, the controller used in the force appropriation experiment would need to operate off the phase of the target mode's response as opposed to that of the drive point accelerometer.

The effect of noise on these damping identification techniques was deemed outside the scope of the current work. These should be explored in future works to determine the sensitivity of these methods to noise on the force and response measurements as well as the mode shape values.

4 Model Definitions

The nonlinear models utilized in this work were chosen to demonstrate how different nonlinear phenomena can affect the amplitude dependent damping ratios using the techniques from Section 3. The three nonlinear systems, shown in Fig. 1, are a softening Duffing oscillator, a contact-gap oscillator, and a single-mass system with a Jenkins element. The Duffing and contact-gap oscillators provide stiffness-only nonlinearities but with different dynamics activated: the former nonlinearity is odd (i.e., $-f(x) = f(-x)$ for all x) while that of the latter is even (i.e., $-f(x) \neq f(-x)$ for all x). These will excite different frequency content (odd harmonics for the Duffing oscillator and both odd and even harmonics for the contact-gap oscillator). The Jenkins oscillator models the effect of Coulomb friction, which is a hysteretic type of nonlinearity dependent on the history of the response. Thus, while these nonlinear systems do not encompass all potential nonlinear physics encountered in practice, they do represent functional forms commonly encountered in structural dynamics. The equation of motion for each is Equation 1 with the corresponding nonlinear forcing function, f_{nl}, given in Table 1 with parameter values listed in Table 2. Each system utilized the first 15 harmonics in the MHB solutions, and the contact-gap and SDOF Jenkins oscillators also included the DC component. The number of harmonics was selected by a convergence study where the number harmonics was incremented and observing the resulting displacement from the MHB computations. For the results presented in this section, phase resonance was maintained only at the fundamental frequency. The following sections discuss each of these systems and MHB results in greater detail.

4.1 Duffing Oscillator

The Duffing oscillator (Fig. 1a) utilizes a cubic spring along with the linear spring and dashpot. The negative sign on the nonlinear forcing shown in the first row of Table 1 will result in the stiffness decreasing as displacement amplitude increases. This represents a stiffness nonlinearity with no dependence on velocity. A sample of the MHB results are given in Fig. 2 which shows the magnitudes of the displacement harmonics versus the fundamental frequency. The resonant frequency decreases with increased response amplitude due to the negative k_{nl} value. Additionally, only odd harmonics are present in the response.

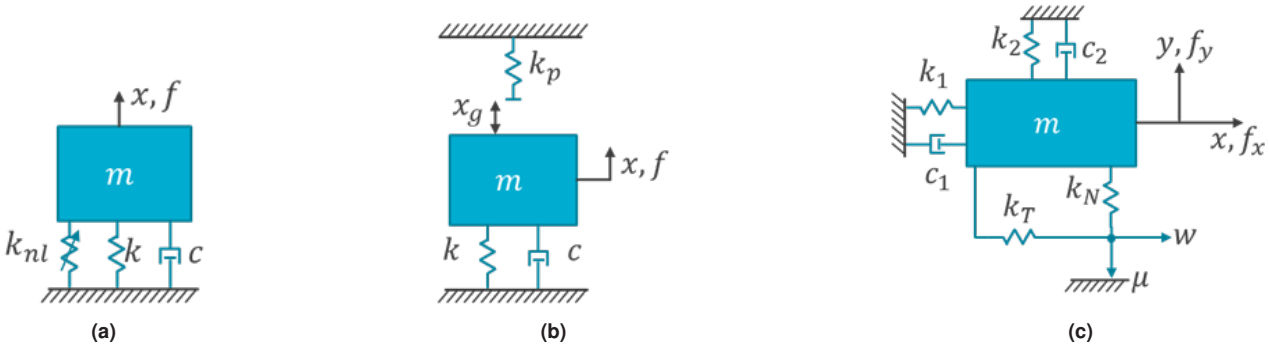

Fig. 1: Nonlinear SDOF systems studied; (a) Duffing oscillator, (b) Contact-gap oscillator, and (c) Jenkins Oscillator

Table 1: Nonlinear Forces for Studied SDOF Systems

System	f_{nl}
Duffing Oscillator	$f_{nl} = -k_{nl}x^3$
Contact Gap Oscillator	$f_{nl} = \begin{cases} 0 & x < x_g \\ k_p\left(x - x_g\right) & x \geq x_g \end{cases}$
Jenkins Oscillator	$f_{nl} = \begin{cases} k_T\left(x - w(t-\Delta t)\right) & y < 0, \lvert k_T(x-w)\rvert < \lvert \mu k_N y\rvert \\ -\mu k_N y \frac{k_T(x-w(t-\Delta t))}{\lvert k_T(x-w(t-\Delta t))\rvert} & y < 0, \lvert k_T(x-w)\rvert \geq \lvert \mu k_N y\rvert \\ 0 & y \geq 0 \end{cases}$

Table 2: Parameters for SDOF Systems

Parameter	Duffing	Contact	Jenkins	Units
m	1	1	1	kg
c	0.05	0.05	—	$N \cdot s/m$
k	1	1	—	N/m
c_1	—	—	0.01	$N \cdot s/m$
c_2	—	—	0.01	$N \cdot s/m$
k_1	—	—	1	N/m
k_2	—	—	1	N/m
k_{nl}	0.5	—	—	N/m^3
k_p	—	5	—	N/m
x_g	—	0.5	—	m
k_N	—	—	100	N/m
k_T	—	—	50	N/m
μ	—	—	0.2	—

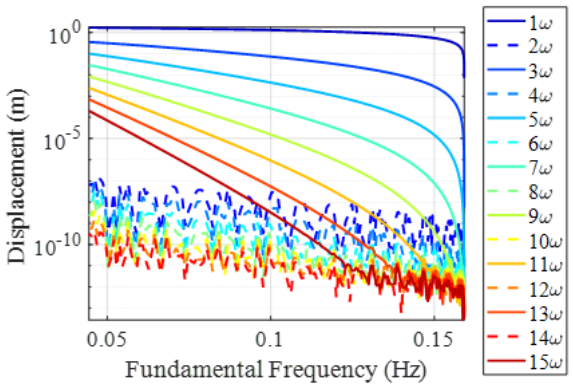

Fig. 2: MHB results for the Duffing oscillator, magnitudes of displacement harmonics versus fundamental frequency

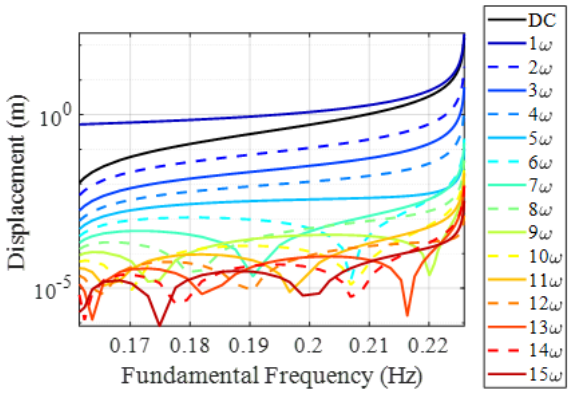

Fig. 3: MHB results for the contact gap oscillator, magnitudes of displacement harmonics versus fundamental frequency

4.2 Contact-Gap Oscillator

The contact gap model represents a system where a portion of the structure comes in and out of contact with a spring during a cycle of oscillation, as shown in Fig. 1b. The physics represented here is an asymmetric contact which engages only during the positive oscillations of displacement. Contact occurs when the displacement exceeds the gap distance signified by x_g, and therefore resulting in a piecewise linear spring as the nonlinear stiffness force (see the second row of Table 1). When the gap is closed, the penalty spring with linear stiffness k_p engages and the total stiffness is the sum of the two springs, $k + k_p$. Note that this model assumes that a contact gap nonlinearity only influences the stiffness, while the damping force remains linear since there is no damping associated with the contact.

A sample of the MHB results are given in Fig. 3 which shows the magnitudes of the displacement harmonics versus the fundamental frequency. The effect of the penalty spring is that the system stiffens as response amplitude is increased. Note that the first solution of MHB had the gap spring in contact so the DC and harmonics magnitudes are immediately present. Unlike the Duffing oscillator, the contact gap excites both even and odd harmonics due to the asymmetric nature of the nonlinearity.

4.3 Single-Mass Oscillator with Jenkins Element

All the systems considered so far have been SDOF. The single-mass oscillator with a Jenkins element (shown in Fig. 1c), is described by two orthogonal DOFs, x and y, and it used to describe the effect of Coulomb friction on a structure. As such, it can capture the effects of frictional slip on a system. The equations of motion are given in Equations 31 and 32 below [31, 32]:

$$m\ddot{y} + c_2\dot{y} + k_2 y + f_N = f_y \tag{31}$$

$$m\ddot{x} + c_1\dot{x} + k_1 x + f_T = f_x \tag{32}$$

where f_N and f_T are the normal and tangential forces generated by the Jenkins element slider and are given by

$$f_N = \begin{cases} k_N y & y < 0 \\ 0 & y \geq 0 \end{cases} \tag{33}$$

$$f_T = \begin{cases} k_T\left(x - w(t-\Delta t)\right) & y < 0, |k_T(x-w)| < |\mu k_N y| \\ -\mu k_N y \frac{k_T(x-w(t-\Delta t))}{|k_T(x-w(t-\Delta t))|} & y < 0, |k_T(x-w)| \geq |\mu k_N y| \\ 0 & y \geq 0 \end{cases} \tag{34}$$

where Δt is the time step, μ is the static coefficient of friction and w is the slider position given by:

$$w(t) = \begin{cases} w(t-\Delta t) & y < 0, f_T < |\mu k_N y| \\ x + \frac{\mu k_N y}{k_T}\left(\frac{f_T}{|f_T|}\right) & y < 0, f_T \geq |\mu k_N y| \\ x & y \geq 0 \end{cases} \tag{35}$$

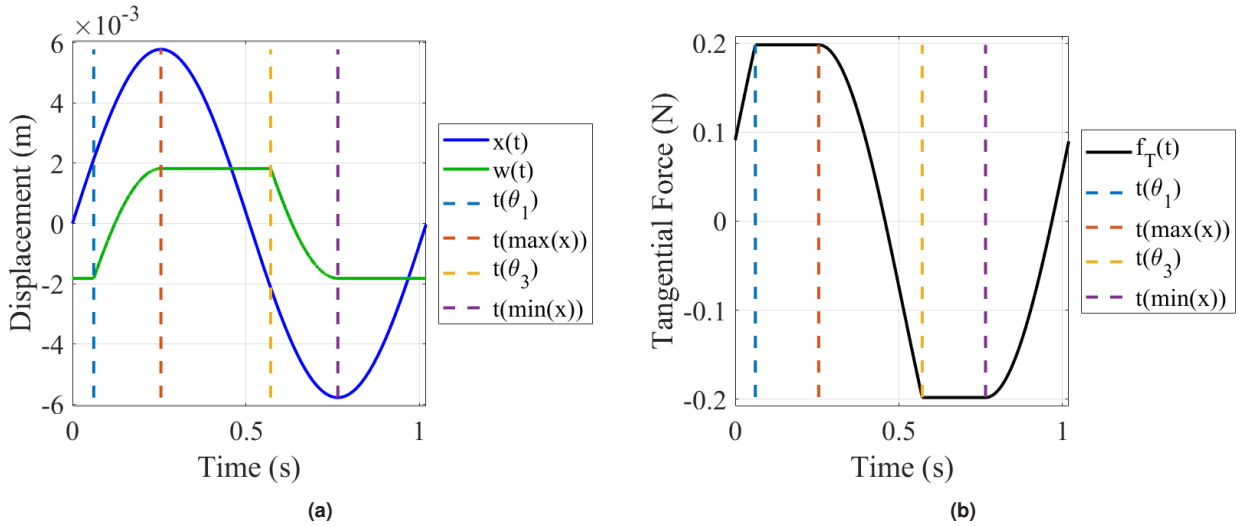

Fig. 4: Notional plot of displacements and tangential force in Jenkins elements; (a) mass and slider displacement and (b) tangential force

For this work, a constant pre-load of $f_N = -1$N was applied in the y-direction such that the slider was engaged, but no dynamic force in y was applied. Since for this system there is no dynamic coupling from x to y (i.e., x motion does not induce y motion), $\ddot{y} = \dot{y} = 0$ and $y = y_0 = -0.0099$. Therefore, the nonlinear force listed in the last row of Table 1 for this system is defined only by Equation 34. The tangential stiffness of the Jenkins element, k_T, is meant to represent the stiffness of the interface when the oscillator is in a stuck state. When the system slips, the tangential stiffness becomes k_1, which is small relative to k_T, such that the oscillator produces stick-slip behavior observed in frictional interfaces.

Figure 4 shows x, w, and f_T for a notional cycle of oscillation for a SDOF system with a Jenkins element that exhibits slip. Slip initiates at times $t(\theta_1)$ and $t(\theta_3)$ where θ is the instantaneous phase angle of the x-direction displacement of the mass. The system returns to a stuck state at times of reversals in the mass displacement x, i.e., $t(\max(x))$ and $t(\min(x))$. The slider displacement is constant when the system is in a stuck state, but then changes with x during times of slip. The reverse is true for the tangential force.

To solve the equations of motion with MHB, the process in [31, 32] was followed which involves solving f_T a predictor-corrector fashion and deriving the Jacobian of the nonlinear forces. Phase resonance was achieved only in the x-direction for x and f_x. A sample of the MHB results are given in Fig. 5 which shows the magnitudes of the displacement harmonics versus the fundamental frequency. The resonant frequency decreases with increased amplitude, which is the typical trend for a friction-type behavior. The frequency content of the displacement only contains odd harmonics. The system is fully stuck and behaves linearly for fundamental displacement amplitudes less than approximately 4mm. In this regime, all harmonics are zero (to numerical noise) and the displacement versus frequency is a vertical line. At displacement amplitudes just over 4mm, the friction force of the slider is overcome, and the system begins to slide, activating the nonlinearity and thus higher harmonics in the response. Additionally, the fundamental frequency begins to decrease with increasing displacement amplitude.

5 Nonlinear Damping Ratios for SDOF MHB Results

The MHB results from Section 4, where phase resonance was achieved only at the fundamental frequency, were used with Equations 9, 25, and 28 to compute the amplitude-dependent damping ratios for the three nonlinear systems presented. The results are plotted in Fig. 6 along with the corresponding linear values. The damping ratios computed from the three different techniques yielded identical values for all three nonlinear systems considered. The reason for this result is that all three nonlinear systems satisfied the criteria listed in Section 3.4 which delineate the conditions under which the three presented damping identification techniques provide identical results. Each starts at or near the linear value at low displacement amplitude and then diverge, either increasing or decreasing in damping ratio. The damping ratio for the Duffing Oscillator (Fig. 6a) and Jenkins element (Fig. 6c) increases as the displacement amplitude increases, whereas that for the contact-gap oscillator (Fig. 6b) decreases. Note that while the Duffing and

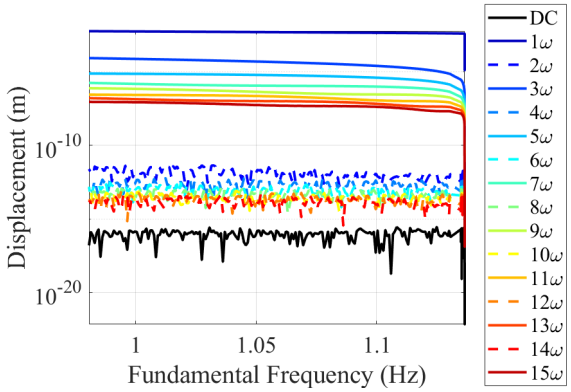

Fig. 5: MHB results for the Jenkins oscillator, magnitudes of displacement harmonics versus fundamental frequency

contact-gap oscillators have exclusively stiffness nonlinearities, damping ratio changes are still observed. This is due to the appearance of frequency (either implicitly or explicitly) in the damping ratio identification equations.

It is noted that the three nonlinear systems considered in this work show large changes in natural frequency and damping (see Figs. 2, 3, 5 and 6). These may not be realistic changes in a practical testing scenario where, e.g., modal interactions could arise with such a large frequency shift. However, since the systems considered are SDOF, the results presented and conclusions reached in this work are still valid.

5.1 Closed Form Solutions

To validate the results of Fig. 6, first order approximations of the nonlinear frequency and damping ratio were computed for each of the nonlinear systems considered. The excitation force and displacement response were assumed to be single harmonic and in phase quadrature:

$$x(t) = X \sin \omega t \tag{36}$$

$$f(t) = F \cos \omega t \tag{37}$$

These expressions were substituted into the equations of motion for the respective nonlinear systems. Expressions for nonlinear frequency and damping ratio were then obtained. For the latter, the EPMC expression for damping ratio in Equation 9 was utilized. Equation 7 can be used to express P_1 in terms of X and F by only including the fundamental components of the drive point velocity and force:

$$P_1 = \frac{\omega X F}{2} \tag{38}$$

Substituting Equation 38 into Equations 8 and 9 and assuming an SDOF system, the first order approximation of damping ratio is obtained:

$$\zeta = \frac{F}{2\omega^2 m X} \tag{39}$$

For each nonlinear system, the amplitude-dependent frequency as well as an expression of F in terms of X are derived by using the equation of motion expanded with x and f as represented in Equations 36 and 37. These are then substituted into Equation 39 to obtain the first order approximation of damping ratio. The following sections detail the process for the Duffing Oscillator (5.2), Contact-Gap Oscillator (5.3), and the SDOF with Jenkins Element (5.4).

Note that the three systems achieved different levels of displacement in the MHB simulations (see Fig. 6). In Sections 5.2 through 5.4, references are made to “low amplitude.” This term is used as a relative measure specific to the system being discussed and corresponds to when the displacement amplitude at which nonlinearity forces are no longer negligible. The “low amplitude” terminology is not meant to compare displacement amplitudes across the three oscillators.

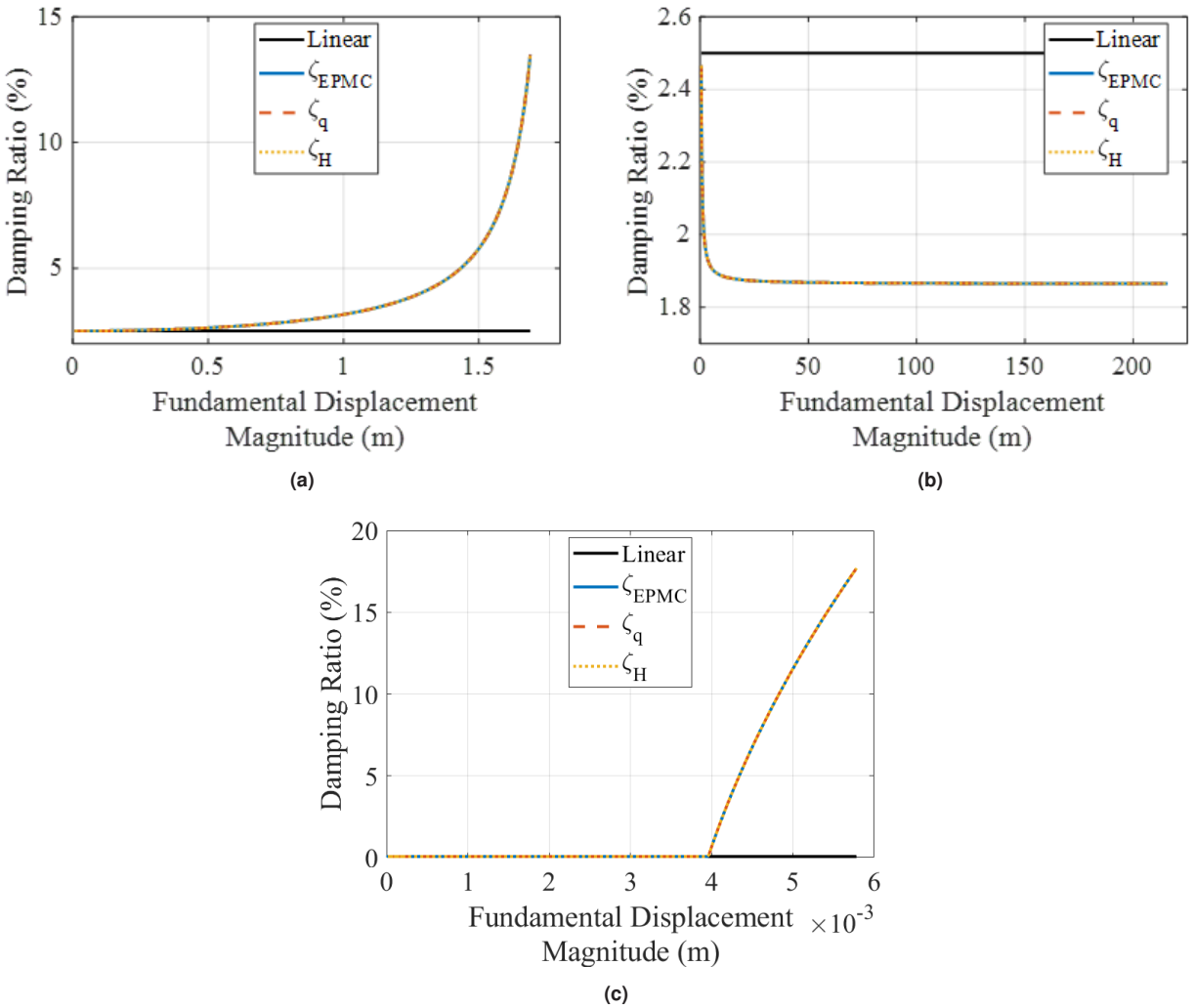

Fig. 6: Amplitude-dependent damping ratios from the nonlinear SDOF systems using MHB results; (a) Duffing oscillator; (b) contact-gap oscillator; (c) single-mass oscillator with Jenkins element

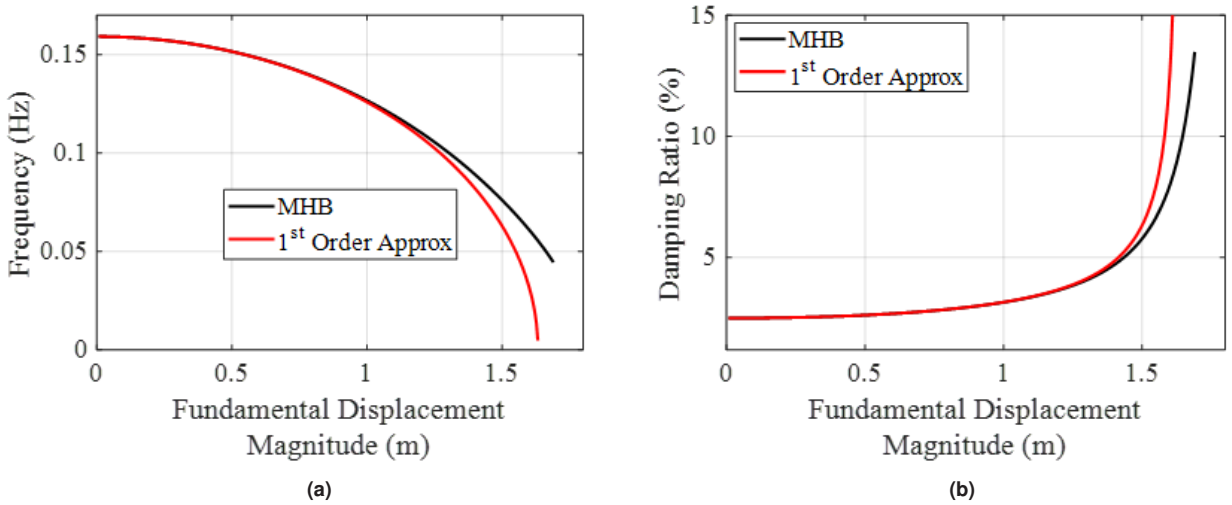

Fig. 7: Comparison of MHB and first order approximations for the Duffing Oscillator; (a) resonant frequency; (b) damping ratio

5.2 Duffing Oscillator

The process used here is similar to that from [39]. Equations 36 and 37 were substituted into Equation 1 with the nonlinear forcing term of the first row of Table 1. The $\sin \omega t$ and $\cos \omega t$ terms were grouped and are shown in Equations 40 and 41, respectively.

$$-m\omega^2 X + kX - \frac{3}{4}k_{nl}X^3 = 0 \tag{40}$$

$$c\omega X = F \tag{41}$$

Equation 40 is used to derive the first order approximation of frequency for the Duffing Oscillator:

$$\omega_{1,duffing} = \frac{\sqrt{4k - 3k_{nl}X^2}}{2\sqrt{m}} \tag{42}$$

The first term is the linear natural frequency and the second term is due to the cubic nonlinearity (note the negative sign indicating that it is softening). At low amplitudes, where X is small, $\omega_{1,duffing}$ is well approximated by the linear natural frequency. As the displacement amplitude increases, the nonlinear effect increases in significance and reduces $\omega_{1,duffing}$. Inserting Equations 41 and 42 into 39 gives the first order approximation of damping ratio:

$$\zeta_{1,duffing} = \frac{c}{\sqrt{m(4k - 3k_{nl}X^2)}} \tag{43}$$

Similar to $\omega_{1,duffing}$, when the displacement magnitude is small, this damping ratio is approximately equal to the linear value. As X increases, the damping ratio does as well. Figure 7 compares the frequency and damping ratio, respectively, obtained using MHB and the first order approximations of Equations 42 and 43. There is good agreement at low amplitudes, but as the displacement amplitude increases, the first order approximations become less accurate and deviate from the MHB curves. Note that for the amplitude ranges considered, the first order approximation of frequency tends to, and drops below, zero, causing the damping ratio to increase to infinity. Therefore, only the results of the first order approximation are shown where frequency is greater than zero. The results of Fig. 7 validate the damping ratio results for the Duffing oscillator shown in Fig. 6a.

5.3 Contact-Gap Oscillator

The process to derive the first order approximations of frequency and damping ratio for the contact-gap oscillator is slightly different than that for the Duffing Oscillator due to the piece-wise nature of the nonlinearity. Note that the

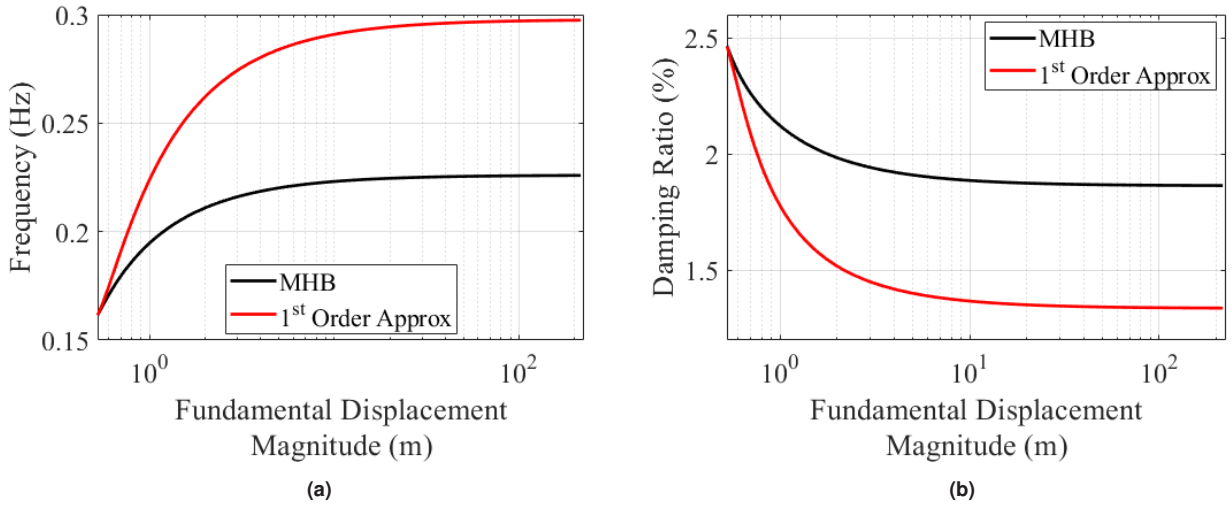

Fig. 8: Comparison of MHB and first order approximations for the Contact-Gap Oscillator; (a) resonant frequency; (b) damping ratio

process described below has similarities with [39] but the overall approach is different. Equations 36 and 37 were substituted into Equation 1 and the linear and nonlinear stiffness forces were combined into a single term:

$$f_s = kx + f_{nl}(x) \approx F_{sc}\cos\omega t + F_{ss}\sin\omega t \tag{44}$$

where $f_{nl}(x)$ is defined by the second row of Table 1.

Equations 36, 37, and 44 were substituted into Equation 1. The $\sin\omega t$ and $\cos\omega t$ terms were grouped and are shown in Equations 45 and 46, respectively.

$$-\omega^2 mX + F_{ss} = 0 \tag{45}$$

$$\omega cX + F_{sc} = F \tag{46}$$

The Fourier Coefficients F_{sc} and F_{ss} are derived in Appendix A. Equations A.6 and A.7 are F_{sc} and F_{ss} for the trivial, linear case when the response is low enough such that the gap remains open throughout the entire fundamental period (i.e., when $X < x_g$). Equations A.11 and A.12 provide expressions for F_{sc} and F_{ss} where the gap closes at some portion through the fundamental period (i.e., when $X \geq x_g$).

Equation 45 is used to solve for the first order approximation of frequency:

$$\omega_{1,contact} = \sqrt{\frac{F_{ss}}{mX}} \tag{47}$$

Inserting Equation 46 into 39, gives the first order approximation of damping ratio:

$$\zeta_{1,contact} = \frac{c}{2\omega_{1,contact}m} = \frac{c\sqrt{X}}{2\sqrt{mF_{ss}}} \tag{48}$$

Figure 8 compares the frequency and damping ratio, respectively, obtained using MHB and the first order approximations of Equations 47 and 48. To highlight the low-amplitude comparison, the fundamental displacement magnitude is provided in log scale. There is good agreement at low amplitudes, but as the displacement amplitude increases, the first order approximations become less descriptive of the system's motion and therefore the deviations from the MHB increase. Figure 3 shows a rapid increase in the harmonics as well as a significant DC term for amplitudes where the gap closes, and therefore the first order approximations are less accurate in these regimes. Given the good agreement at low amplitudes where Equation 36 more accurately represents the response, the results of Fig. 8 validate the damping ratio results for the contact-gap shown in Fig. 6b.

5.4 SDOF with Jenkins Element

The SDOF model with the Jenkins element focuses on capturing the motion in the transverse, x-direction, as the preload was applied in the y-direction such that $y = y_0 < 0$, to engage the slider. No dynamic force was applied in the y-direction and there is no dynamic coupling between x and y (i.e., x motion does not induce y motion) for this system, so it is fair to assume $\dot{y} = \ddot{y} = 0$. Under this assumption, the Jenkins single-mass oscillator was considered to be SDOF in the x-direction.

The approach to derive the first order approximations of frequency and damping ratio is similar to the method that was used for the contact-gap oscillator. The equation of motion for the SDOF with Jenkins Element in the x-direction is written as:

$$m\ddot{x} + c_1\dot{x} + k_1 x + f_T = f_x \tag{49}$$

where f_T is the tangential force from the Jenkins element and is defined in Equation 34 (the last row of Table 1). It is approximated as a single-frequency signal:

$$f_T = F_{Tc}\cos\omega t + F_{Ts}\sin\omega t \tag{50}$$

where F_{Tc} and F_{Ts} are Fourier Coefficients derived in Appendix B. Equations B.6 and B.7 are F_{Tc} and F_{Ts} for the trivial, linear case when the response is low enough such that the slider remains stuck through the entire fundamental period. Equations B.10 and B.11 provide expressions for F_{Tc} and F_{Ts} where the slip occurs at some portion through the fundamental period.

Equations 36, 37, and 50 were substituted into Equation 32. The $\sin\omega t$ and $\cos\omega t$ terms were grouped and are shown in Equations 51 and 52, respectively, where, for each MHB solution, the appropriate tangential Fourier Coefficients (stuck vs slip) are used depending on whether the system slips at any point throughout the fundamental period.

$$-\omega^2 mX + k_1 X + F_{Ts} = 0 \tag{51}$$

$$\omega c_1 X + F_{Tc} = F \tag{52}$$

Equation 51 is used to solve for the first order approximation of frequency:

$$\omega_{1,Jenkins} = \sqrt{\frac{k_1 X + F_{Ts}}{mX}} \tag{53}$$

Inserting Equation 52 into 39, gives the first order approximation of damping ratio:

$$\zeta_{1,Jenkins} = \frac{\omega_{1,Jenkins} c_1 X + F_{Tc}}{2\omega_{1,Jenkins}^2 mX} \tag{54}$$

Figure 9 compares the frequency and damping ratio, respectively, obtained using MHB and the first order approximations of Equations 53 and 54. There is good agreement at low amplitudes, but as the displacement amplitude increases, the first order approximations become less accurate and therefore the deviations from the MHB increase. The results of Fig. 9 validate the damping ratio results for the Jenkins SDOF shown in Fig. 6c.

6 Effect of Higher Harmonics in Phase Resonance

The previous sections assumed that forcing was only applied at the fundamental frequency. This section uses MHB to explore the damping ratio results when higher harmonics are present in force for two scenarios. One scenario is an idealized case where phase resonance is enforced at all active higher harmonics as well as the fundamental frequency and in the subsequent section is referred to as the "multi-harmonic primary phase resonance" (MPPR) case. The harmonic balance solutions were recomputed with forcing applied to the harmonics which were shown to be excited in Section 5 and constraints enforcing phase resonance on a per-harmonic basis [28].

The second scenario replicates practical experimental conditions by including an electromechanical model of a modal shaker (see Fig. 10) attached to the SDOF system in the MHB computations and maintains phase resonance at

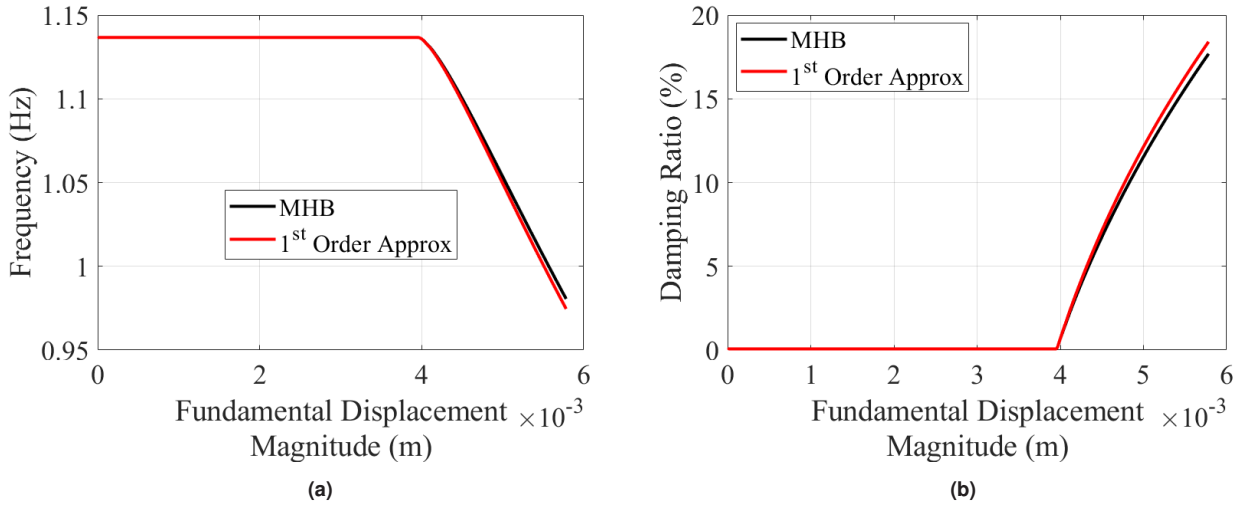

Fig. 9: Comparison of MHB and first order approximations for the SDOF with Jenkins Element; (a) resonant frequency; (b) damping ratio

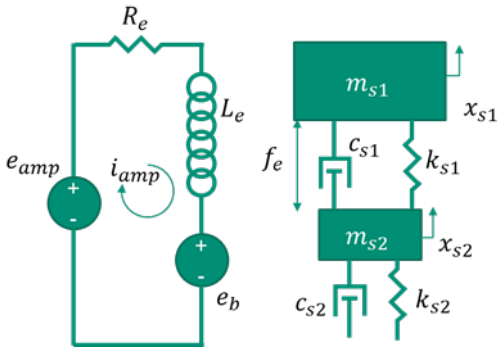

Fig. 10: Electromechanical model of modal shaker [30]

only the fundamental frequency [29]. This is referred to as the "experimental conditions" (EC) case in the subsequent sections. The shaker was attached to the mass of each SDOF via spring k_{s2} and damper c_{s2}. The shaker parameters were taken directly from [30] and represent an MB Dynamics Modal 50A shaker and Labworks PA-138 amplifier. The output voltage from the DAQ is the input parameter and forcing into the SDOF is a function of the oscillator's response as well as that of the shaker armature based on k_{s2} and damper c_{s2}. Therefore, any harmonics produced by the nonlinearity manifest in the force but are uncontrolled. This scenario thus captures shaker-structure interactions that can occur during force appropriation testing of nonlinear structures [30].

In the sections that follow, the MHB solutions are computed for the two above scenarios and compared against the baseline results from Section 4 of single input forcing with phase resonance achieved at only the fundamental frequency. For all scenarios, while forcing is present at higher harmonics, Equations 9, 25, and 28 utilize only the fundamental components of forcing and response for the damping ratio identification.

6.1 Duffing Oscillator

Based on the results in Fig. 2, the MPPR case for the Duffing Oscillator maintained phase resonance at all odd harmonics up to index 15. Figure 11 shows MHB results for the baseline, MPPR, and EC scenarios considered. The displacement responses for the baseline and MPPR case were similar, so Fig. 11a only shows the magnitudes of the displacement harmonics for the baseline case. Figure 11b shows that the higher harmonic content of displacement for the EC case is notably different than the results of the other two cases. Figures 11c through 11e show that all three scenarios resulted in different forces at the higher harmonics as well as the fundamental frequency. The disparities in the harmonics are to be expected given the different forcing conditions associated with each scenario. The single-tone

and multi-harmonic forcing of the baseline and MPPR cases, respectively, are clearly visible from Fig. 11c and 11d. The effects of shaker-structure interactions are manifest in Figs. 11e and 11f where the uncontrolled higher harmonics do not achieve phase resonance and notably differ from the MPPR case in magnitude (note that data shown in Fig. 11f is only included for those solutions where the force was sufficiently above the numerical noise floor; the 15^{th} harmonic is not shown as it never reached this threshold).

The effect of these differences in displacement and forcing on the identified damping ratio is now discussed. Since the conditions of Section 3.4 are still met for each of the three scenarios, all the damping ratio identification techniques yield the same results. Therefore, for brevity, only the EPMC results will be shown (Eq. 9). Figure 12a shows the damping ratio identified from the Duffing Oscillator MHB results for the three scenarios considered. All three emanate from the linear value at low response amplitude and all begin to increase. However, the damping ratio estimates for all three cases diverge as the response amplitude increases.

To explain these differences, the various terms of Equations 8 and 9 are considered. The amplitude-dependent terms in these equations are the fundamental component of excitation force as well as the resonant frequency (the displacement is considered the independent variable in this discussion). These two parameters are plotted in Figs. 12b and 12c for the three scenarios considered. The resonant frequency for the baseline and MPPR cases agreed well as shown in Fig. 12c, but there is a clear difference in the EC result, further demonstrating the distortions arising from shaker-structure interaction. Figure 12b shows a large variation in the fundamental excitation force for the three cases. Given the difference in the frequency and fundamental forcing for the EC results, the reason for the variation in the corresponding damping ratio behavior relative to the other two cases is clear. The resonant frequency for the baseline and MPPR cases is similar, therefore the differences in the damping ratios between these two cases in Fig. 12a is attributed to the corresponding differences in the fundamental forcing.

The comparison of the above results for the baseline and MPPR cases indicate that having higher harmonics in phase resonance can influence the fundamental forcing and therefore the damping ratio. To understand this behavior, a second order approximation of the Duffing Oscillator equation of motion is used. A similar process to Section 5.1 is repeated here with the exception that the third harmonic is included so that the assumed displacement and force are:

$$x(t) = X_1 \sin \omega t + X_{3,c} \cos 3\omega t + X_{3,s} \sin 3\omega t \tag{55}$$

$$f(t) = F_1 \cos \omega t + F_{3,c} \cos 3\omega t + F_{3,s} \sin 3\omega t \tag{56}$$

The primary phase resonance is shown to be achieved at the fundamental frequency, but not necessarily at the third harmonic. Equations 55 and 56 are inserted into Equation 1 with f_{nl} defined by the first row of Table 1 and only the first and third harmonics are balanced. This results in four equations:

$$kX_1 - m\omega^2 X_1 - \frac{3}{4}k_{nl}X_1^3 - \frac{3}{2}k_{nl}X_1X_{3,c}^2 + \frac{3}{4}k_{nl}X_1^2X_{3,s} - \frac{3}{2}k_{nl}X_1X_{3,s}^2 = 0 \tag{57}$$

$$c\omega X_1 + \frac{3}{4}k_{nl}X_1^2X_{3,c} = F_1 \tag{58}$$

$$\frac{1}{4}k_{nl}X_1^3 - 3c\omega X_{3,c} + kX_{3,s} - 9m\omega 2X_{3,s} - \frac{3}{2}k_{nl}X_1^2X_{3,s} - \frac{3}{4}k_{nl}X_{3,c}^2X_{3,s} - \frac{3}{4}k_{nl}X_{3,s}^3 = F_{3,s} \tag{59}$$

$$3c\omega X_{3,s} + \left(k - 9m\omega^2 - \frac{3}{2}k_{nl}X_1^2 - \frac{3}{4}k_{nl}X_{3,c}^2 - \frac{3}{4}k_{nl}X_{3,s}^2\right)X_{3,c} = F_{3,c} \tag{60}$$

These equations are strongly coupled in the response harmonics X_1, $X_{3,s}$, and $X_{3,c}$. When phase resonance is achieved at the first and third harmonics, $F_{3,s} = X_{3,c} = 0$, $F_1 = c\omega X_1$ (Equation 58), and $F_{3,c} = 3\omega c X_{3,s}$ (Equation 60) indicating that the damping forces are balanced at both the fundamental and third harmonics. However, if phase resonance is only achieved at the fundamental frequency, $F_{3,s} = F_{3,c} = 0$, and the damping associated with the third harmonic is balanced via Equation 60 by forcing $X_{3,c}$ to be non-zero. This results in a distortion of $\frac{3}{4}k_{nl}X_1^2X_{3,c}$ added to the fundamental forcing according to Equation 58 since $X_{3,c} \neq 0$. Therefore, when phase resonance is not achieved at higher harmonics, the forcing at the frequencies where phase resonance is achieved accounts for the

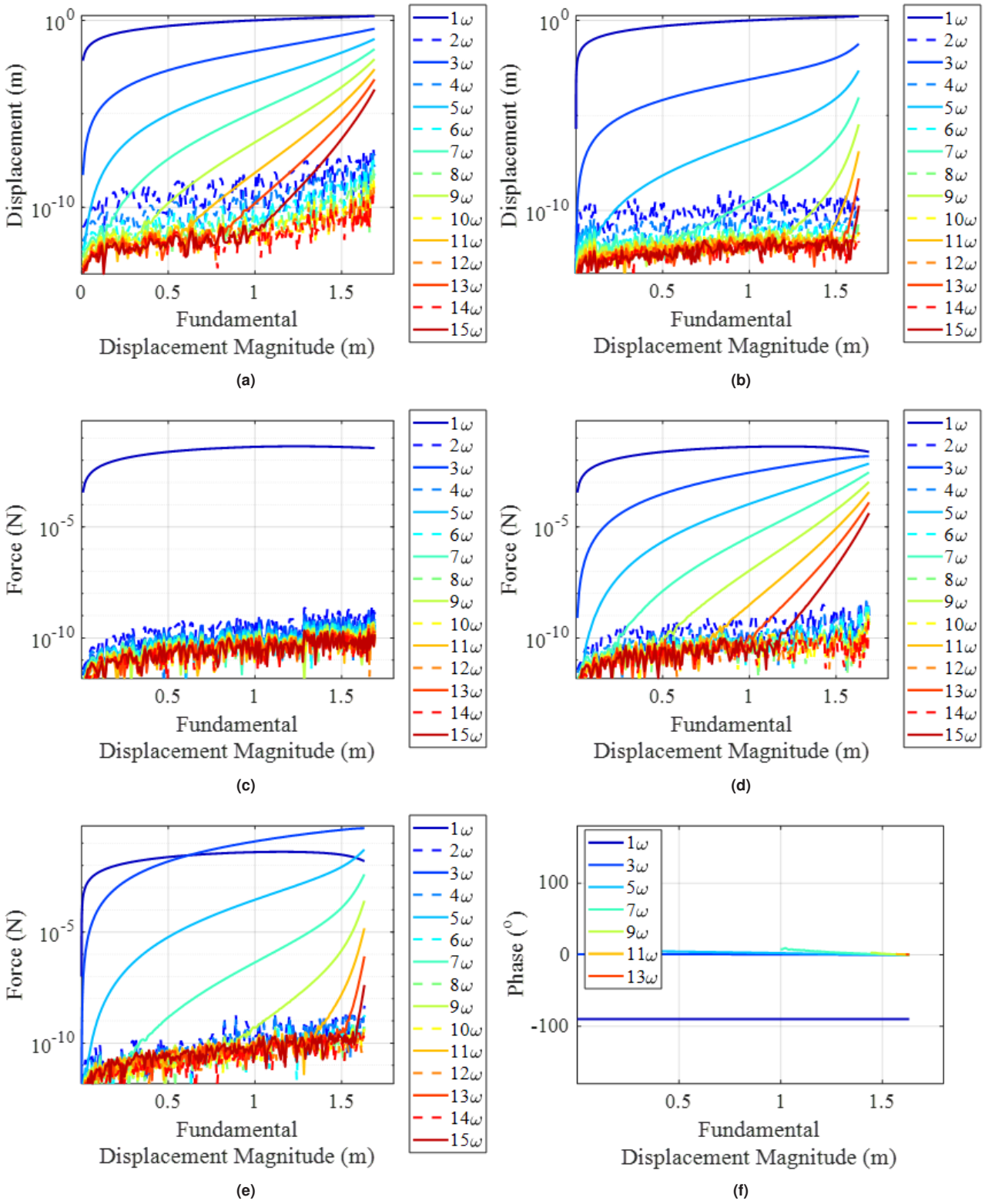

Fig. 11: MHB results for the Duffing Oscillator for different scenarios. Displacement for the (a) baseline and MPPR cases and (b) the EC case; (c) excitation force for the baseline case; (d) excitation force for the MPPR case; (e) excitation force and (f) displacement-force relative phases for the EC case

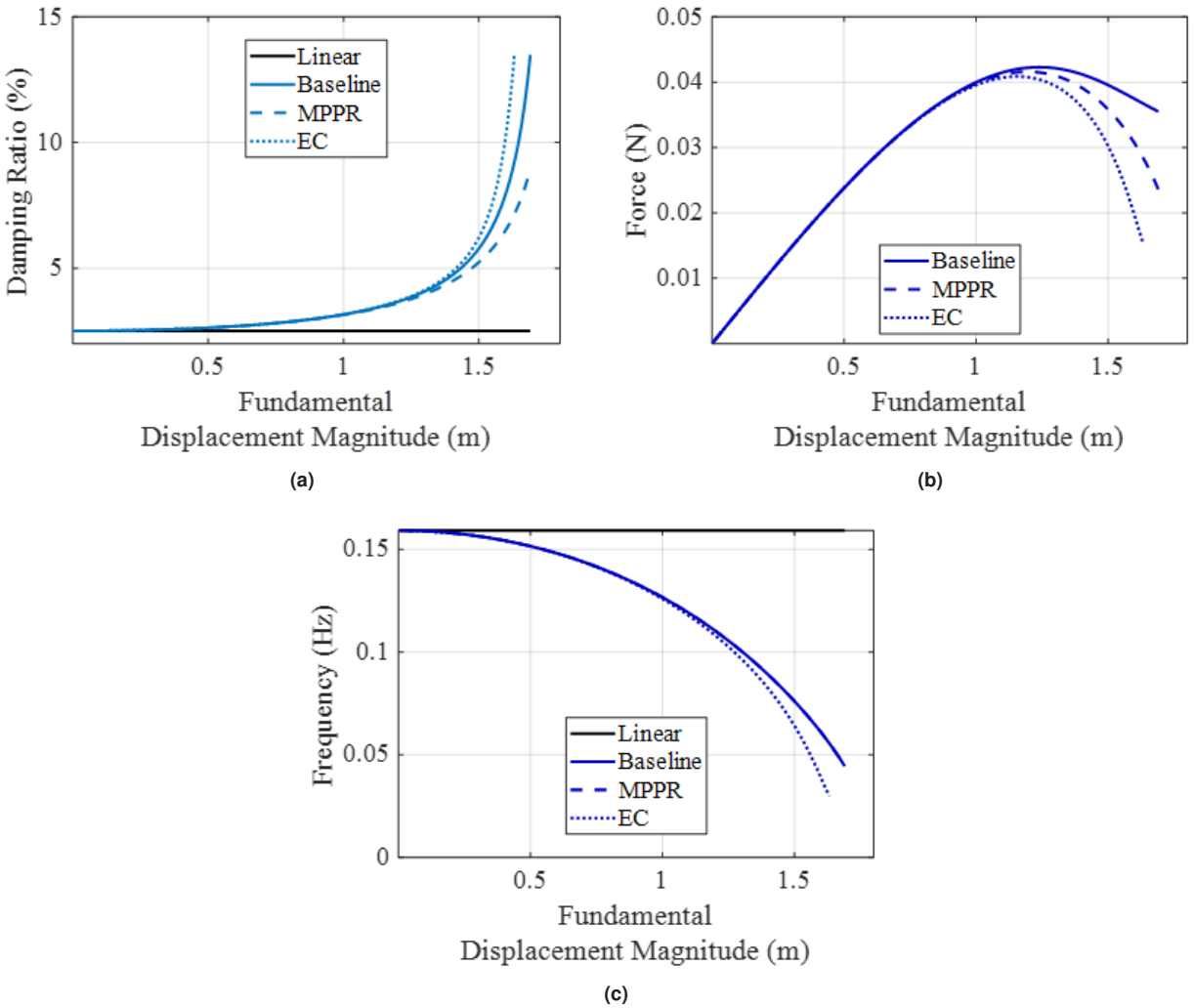

Fig. 12: Comparisons of parameters for the Duffing Oscillator MHB solutions for different scenarios; (a) damping ratio, (b) fundamental excitation force, and (c) frequency

additional dissipation associated with the higher harmonics. These mechanics are further exacerbated when there are uncontrolled higher harmonics as in the EC case since both $F_{3,s}$ and $F_{3,c}$ are likely to be non-zero.

These trends are seen in both Figs. 11 and 12. Because phase resonance is only achieved at the fundamental force for the baseline case, the fundamental force at the phase resonance condition differs from the ideal MPPR case (Figs. 11c, 11d, and 12b). Therefore, the damping ratio for these two cases differ. Additionally, the EC case has higher harmonics in the forcing (Fig. 11e), but none are in phase resonance (Fig. 11f). These distort the F_1 (Fig. 11e and Fig. 12b) and the fundamental frequency (Fig. 12c) at which phase resonance occurs. With these differences, the damping ratio from the EC case thus deviates from the other two cases (Fig. 12a). These results, corroborated through the second order analytical solution above, show a sensitivity of the identified damping ratio to the phase resonance conditions, specifically the forcing harmonics maintained in phase resonance.

Note that, while this example resulted in the fundamental force increasing when the forcing harmonics were not in-phase resonance (excluding the EC case since this result also involves shaker-structure interactions), there could be scenarios where the opposite is true. The effect of the forcing harmonic coupling and the corresponding change in the identified damping ratio will depend on the form of the nonlinearity.

6.2 Contact-Gap Oscillator

The process described above for the Duffing Oscillator is repeated for the Contact-Gap Oscillator. Based on Fig. 3, the MPPR case for the Contact-Gap Oscillator maintained all harmonics in phase resonance. In-depth MHB results are not presented here for brevity since the general observations between the different scenarios are similar to those from the Duffing Oscillator. Specifically, the displacement frequency content for the baseline and MPPR cases all agreed well, and the DC and higher harmonics for the EC were notably different from the former two scenarios due to shaker-structure interactions. Additionally, the frequency content of the excitation force were in disagreement between all three scenarios, the largest differences occurring at the higher harmonics: only the fundamental component of force is active for the baseline case (by definition); all forcing harmonics are active and in primary phase resonance for the MPPR case; and all forcing harmonics are active but primary phase resonance only occurring at the fundamental component for the EC case.

Figure 13 shows a selection of the MHB results for the three scenarios for the Contact-Gap Oscillator: the damping ratio identified using the EPMC framework in Eq. 9 (Fig. 13a), the fundamental component of the excitation force (Fig. 13b), and the fundamental resonant frequency (Fig. 13c). The trends observed are all similar to those of the Duffing Oscillator. The damping ratio identified from each case differs. The frequency for the baseline and MPPR is similar, but that of the EC is distorted from the shaker-structure interactions. Lastly, the fundamental excitation force is different for all three cases. These results corroborate the findings for the Duffing Oscillator where achieving phase resonance at the higher harmonics alters the fundamental forcing, resulting in differences in the identified damping ratio. Additionally, uncontrolled forcing harmonics due to shaker structure interaction similarly distort the identified damping ratio.

6.3 SDOF with Jenkins Element

The process is lastly repeated for the Jenkins Oscillator to demonstrate that the identified damping ratio trend changes depending on the forcing harmonics. Based on the results from Fig. 5, the MPPR case for the Jenkins Oscillator was conducted with maintaining all odd harmonics in phase resonance. Figure 14 shows the relevant results for the three scenarios for the Jenkins Oscillator: the damping ratio identified using the EPMC framework in Eq. 9 (Fig. 14a), the fundamental excitation force magnitude (Fig. 14b), and the fundamental resonant frequency (Fig. 14c). Unlike the previous two systems where significant differences were observed for damping ratio, fundamental force and frequency, the differences in all the parameters for the Jenkins Oscillator are much less between the three cases.

To explain this apparent change in trend, the strength of the displacement harmonics relative to the fundamental are evaluated. Figure 15 plots the displacement magnitudes of the higher harmonics normalized by the fundamental component for each MPPR case of the three nonlinear SDOFs. The displacement harmonics for the Duffing and Contact-Gap Oscillators (Fig. 15a and 15b, respectively) are much more pronounced relative to their respective fundamental components than that seen for the Jenkins Oscillator (Fig. 15c). Recall from Section 6.1 that the difference in damping ratio trends when higher harmonics are in phase resonance is due to the reduced burden of the fundamental forcing to balance the damping associated with these harmonics. Therefore, if the displacement harmonics are not significant relative to the fundamental, then these higher harmonics will minimally influence the damping ratio. Thus, considering the results of Fig. 15c, minimal damping ratio variation is observed for the Jenkins SDOF Oscillator when more harmonics are maintained in phase resonance due to the relatively insignificant

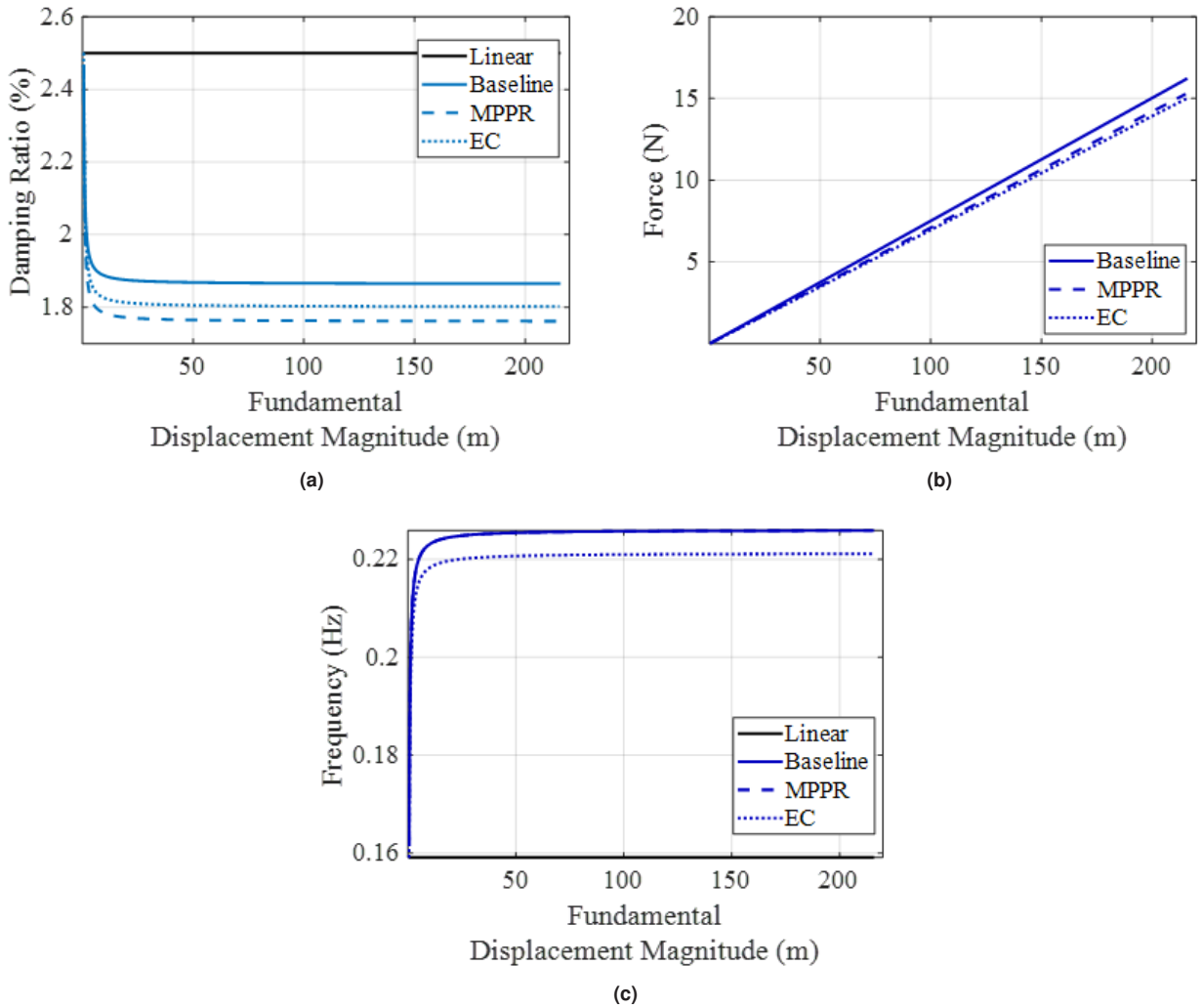

Fig. 13: Comparisons of parameters for the Contact-Gap Oscillator MHB solutions for different scenarios; (a) damping ratio, (b) fundamental excitation force, and (c) frequency

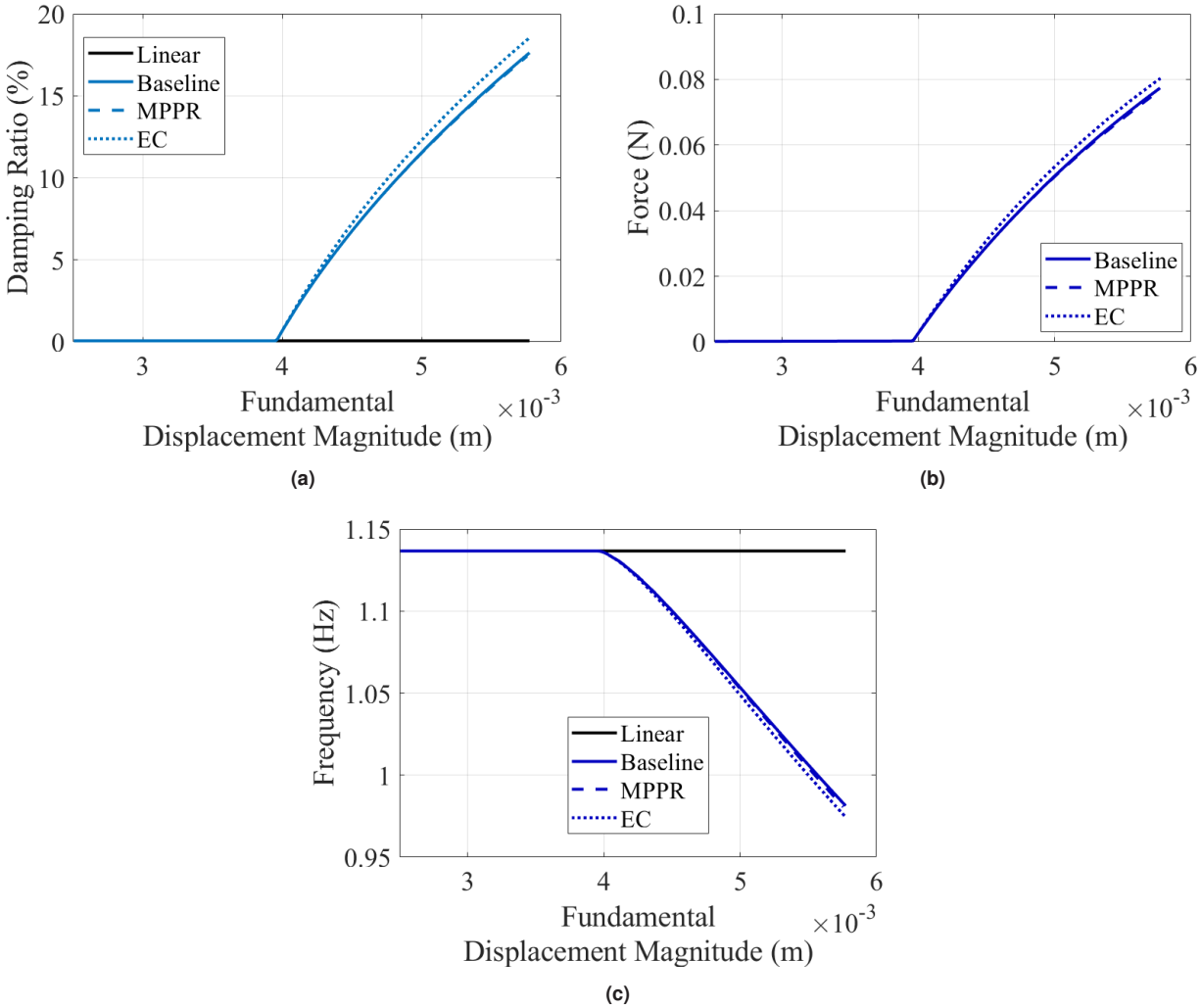

Fig. 14: Comparisons of parameters for the SDOF Jenkins Oscillator MHB solutions for different phase resonance scenarios; (a) damping ratio, (b) fundamental excitation force, and (c) frequency

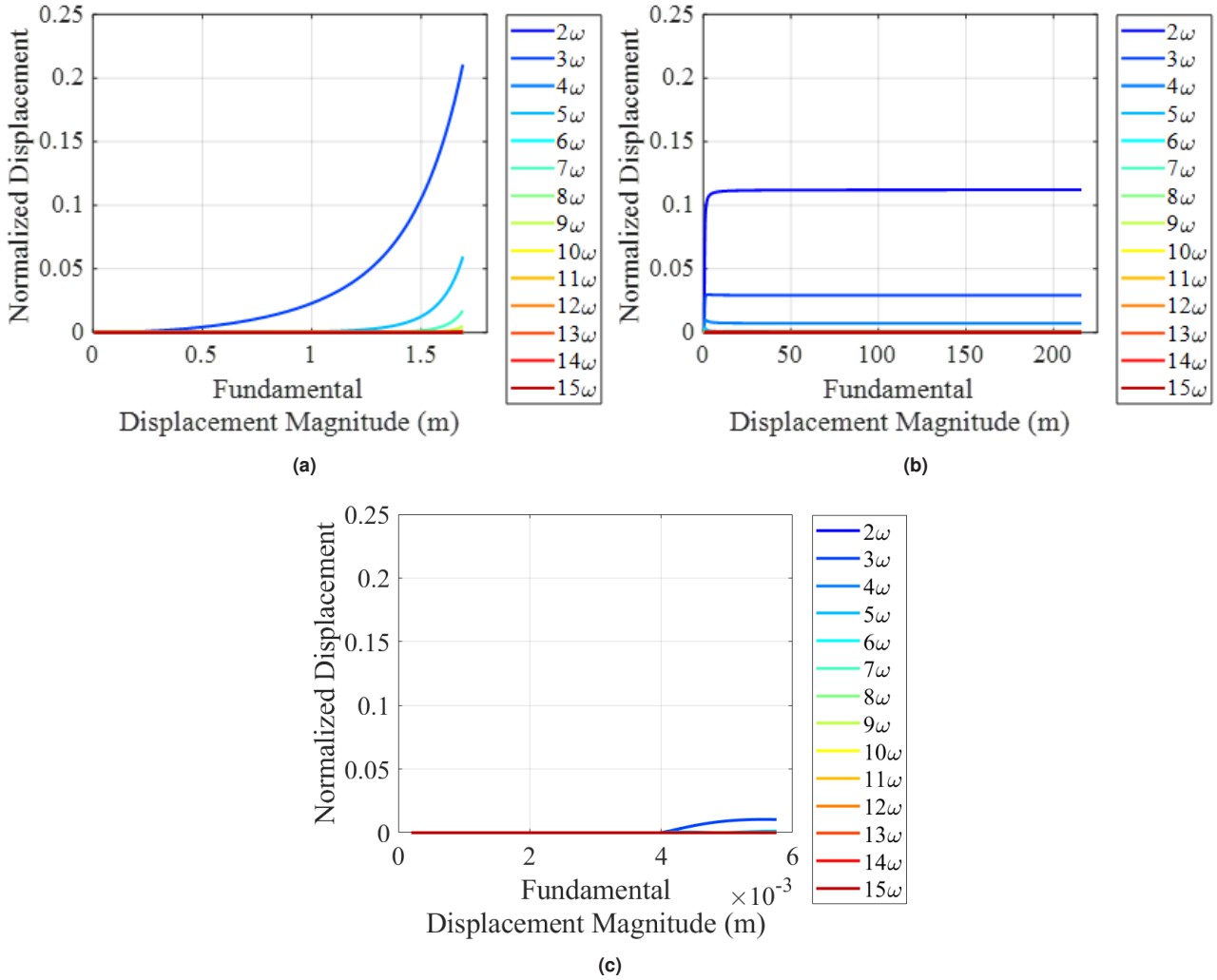

Fig. 15: Magnitudes of the displacement higher harmonics normalized by the fundamental component for (a) Duffing Oscillator where all odd harmonics are maintained in phase resonance, (b) Contact-Gap Oscillator with all harmonics in phase resonance, and (c) SDOF Jenkins Oscillator with all odd harmonics in phase resonance

magnitudes of the displacement harmonics. Similar results are found when the displacement harmonics are evaluated for the EC case.

While the displacement harmonics for the Jenkins EC case do not exactly match its baseline counterpart, the comparison is much closer than the corresponding comparisons for the other two systems. Therefore, given the greater similitude and the relative weakness of the displacement harmonics of the Jenkins EC case, all parameters from all three cases shown in Fig. 14 match better than those from the Duffing and Contact-Gap Oscillators.

7 Conclusions

This work explored limitations of damping ratio identified from nonlinear force appropriation experiments of structures. Three different identification methods were implemented and discussed: one based on the Extended Periodic Motion Concept framework, one based on modal power, and the last utilizes the linear accelerance frequency response function. Multi-harmonic balance was used to conduct virtual experiments on three different single-degree-of-freedom nonlinear oscillators. Data typically available from a force appropriation experiment were extracted from the multi-harmonic balance results and input into the three algorithms to identify the damping ratio.

All three identification techniques generated the same result and will always do so if the following conditions are satisfied: the mode shapes of the structure do not change with response amplitude, the target mode dominates the

response, and single input forcing is used during the nonlinear force appropriation test. All of these were met in the systems explored in this work. However, each technique has specific limitations in their practical implementation. The modal power and FRF techniques are limited to cases where the mode shapes are constant with response amplitude (EPMC allows for changing mode shapes). The EPMC and modal power methods require a sufficiently populated mode shape matrix, limiting their utility to cases with enough instrumentation freedom to independently observe the modes within the bandwidth of interest. The FRF technique needs one input and one output measurement. Therefore, while the three techniques can give the same result, the particular use case will determine which should be used.

The sensitivity of the identified damping ratio to higher harmonics in the excitation force was also explored using the same three nonlinear SDOF oscillators. The higher harmonics in force were introduced in the MHB computations in two different ways. The first applied constraints in the MHB process to enforce phase resonance at harmonics excited by the nonlinearity. The second method incorporated a electromechanical model of a modal shaker into the MHB equations of motion. The excitation force then becomes a response parameter. Constraints were applied in the MHB which enforced primary phase resonance at the fundamental frequency. However, the higher harmonics in the excitation force in this latter case were uncontrolled and were the result of shaker-structure interaction, a phenomenon commonly encountered during actual force appropriation experiments. Both of the MHB cases demonstrated that, whether controlled or uncontrolled, higher harmonic forces influenced the fundamental forcing magnitude. Previous works have shown the insensitivity of frequency and mode shape to imperfect force appropriation (i.e., achieving phase resonance at only a single point and the fundamental harmonic) [13]. However, this work demonstrates that the damping ratio is much more sensitive to the phase resonance conditions achieved during test.

When the higher harmonic forces were controlled to be in phase resonance with their corresponding displacement harmonic, the higher harmonic forces effectively alleviate the burden on the fundamental forcing to balance the damping caused by the higher harmonic responses. When the forcing harmonics are uncontrolled, they distort the fundamental forcing through similar harmonic-coupling mechanisms. Since all three damping ratio identification techniques rely on the fundamental component of the force and response, this change in the fundamental force affects the resulting damping ratio estimates. Therefore, regardless of the technique used, the damping ratio identified from a force appropriation test will differ depending on the harmonics in the excitation force, regardless of whether or not they are controlled to be in phase resonance.

Note that the above sensitivity of the damping ratio estimate is related to the strength of the harmonics in the response. If the magnitudes of the higher harmonics are low relative to the fundamental, then the change in damping ratio estimates are expected to not differ when changing which harmonics are in phase resonance. However, the threshold signifying when a harmonic is large enough to influence the identified damping ratio cannot be known a priori and is not trivial to confidently determine. It is recommended that the sensitivity of the identified damping ratio be explored when utilizing any of the techniques described herein to ensure the damping ratio has been accurately captured.

While this work utilized SDOF systems, the techniques and results presented herein can easily extend to multi-degree of freedom systems. The damping ratio derivations discussed in Sections 3.1 to 3.3 have no restriction on DOFs. In fact, the EPMC and modal power methods require the use of multiple measurement DOFs to provide accurate results (for the computation of the experimental mass and modal filter, respectively). Per Section 3.4, the behavior of the mode of interest will determine the most appropriate damping identification technique to use (e.g., if the mode shapes are observed to change, the most appropriate technique to use to identify damping ratio is the EMPC method). The trends and observations from the multi-harmonic study of Section 6 also extend to (and are exacerbated by) multi-DOF structures. When large harmonics are active in multi-DOF structures, there is the potential for modal interactions and coupling to further obfuscate the identified damping ratios.

Given the sensitivities of the identified damping ratio described above, its use in practice should be used judiciously. Different forcing scenarios should be applied in the force appropriation experiments, and the corresponding identified damping ratios compared to understand the variability with forcing harmonics. Based on these results from this work, it is recommended that multi-harmonic control is used to achieve phase resonance at all significant harmonics in order to obtain the most consistent damping ratio between test and analysis. Additionally, the damping ratio trends should not be conflated with nonlinear damping forces. The Duffing and contact-gap oscillators had purely stiffness nonlinearities yet showed changes in nonlinear damping ratio. Therefore, a change in damping ratio does not indicate the presence of a nonlinear damping force. These identified limitations of nonlinear damping ratios identified from nonlinear force appropriation experiments demonstrate that these quantities should be used thoughtfully.

Appendix

A First Order Approximations of Contact-Gap Oscillator

This appendix provides the mathematical details for computing the Fourier Coefficients of the first-order-approximation of the nonlinear force for the contact-gap oscillator for Section 5.3. The Fourier Coefficients F_{sc} and F_{ss} are computed from

$$F_{sc} = \frac{1}{\pi}\int_0^{2\pi} f_s(\theta)\cos\theta d\theta \tag{A.1}$$

$$F_{ss} = \frac{1}{\pi}\int_0^{2\pi} f_s(\theta)\sin\theta d\theta \tag{A.2}$$

where f_s is defined by Equation 44 and $\theta = \omega t$. The stiffness function depends on whether the gap closes at any portion throughout the oscillation at the fundamental period:

$$f_s(\theta) = \begin{cases} f_{s,o}(\theta) & X < x_g \\ f_{s,c}(\theta) & X \geq x_g \end{cases} \tag{A.3}$$

where the o and c subscripts indicate, respectively, that the gap remains open throughout the entire oscillation or that it closes during some portion of the oscillation. Thus, the Fourier Coefficients of the stiffness force are similarly piecewise:

$$F_{sc} = \begin{cases} F_{sc,o} & X < x_g \\ F_{sc,c} & X \geq x_g \end{cases} \tag{A.4}$$

$$F_{ss} = \begin{cases} F_{ss,o} & X < x_g \\ F_{ss,c} & X \geq x_g \end{cases} \tag{A.5}$$

When $X < x_g$, the gap remains open throughout the entire oscillation and the corresponding stiffness is designated $f_{s,o}(\theta) = kx$, the purely linear case. Substitution of this expression for $f_s(\theta)$ in the integrals of Equations A.1 and A.2 yield the corresponding stiffness force Fourier Coefficients

$$F_{sc,o} = 0 \tag{A.6}$$

$$F_{ss,o} = kX \tag{A.7}$$

For $X \geq x_g$, the gap closes during some portion of the oscillation, and the stiffness force $f_{s,c}(\theta)$ is a piece-wise function [39]

$$f_{s,c}(\theta) = \begin{cases} (k+k_p)x(\theta) - k_p x_g & \theta_1 \leq \theta \leq \theta_2 \\ kx(\theta) & Otherwise \end{cases} \tag{A.8}$$

where θ_1 and θ_2 are the phases corresponding to the closing and re-opening of the gap, respectively, and can be computed as [39]:

$$\theta_1 = \sin^{-1}\left(\frac{x_g}{X}\right) \tag{A.9}$$

$$\theta_2 = \pi - \theta_1 \tag{A.10}$$

The Fourier Coefficients $F_{sc,c}$ and $F_{ss,c}$ are solved in three segments: 0 to θ_1, θ_1 to θ_2, and θ_2 to 2π. Performing the integrations of Equations A.1 and A.2 with $f_{s,c}(\theta)$ for $f_s(\theta)$, the corresponding stiffness force Fourier Coefficients are:

$$F_{sc,c} = 0 \tag{A.11}$$

$$F_{ss,c} = kX + \frac{k_p X}{\pi}\left(\frac{\pi}{2} - \theta_1 + \frac{1}{2}\sin 2\theta_1\right) - \frac{2k_p x_g}{\pi}\cos\theta_1 \tag{A.12}$$

B First Order Approximations of SDOF Jenkins Oscillator

This appendix provides the mathematical details for computing the Fourier Coefficients of the first-order-approximation of the nonlinear force for the Jenkins oscillator for Section 5.4 and is analogous to that done in [40] and [41]. The Fourier Coefficients F_{Tc} and F_{Ts} are computed from

$$F_{Tc} = \frac{1}{\pi}\int_0^{2\pi} f_T(\theta)\cos\theta d\theta \tag{B.1}$$

$$F_{Ts} = \frac{1}{\pi}\int_0^{2\pi} f_T(\theta)\sin\theta d\theta \tag{B.2}$$

where f_T is given in Equation 50 and $\theta = \omega t$. The tangential stiffness force used in these integrations is based on whether the response amplitude is sufficiently high to induce slip at some portion throughout the fundamental period:

$$f_T(\theta) = \begin{cases} f_{T,st}(\theta) & k_T\,(X - \max(w)) < |\mu k_N y_0| \\ f_{T,sl}(\theta) & k_T\,(X - \max(w)) \geq |\mu k_N y_0| \end{cases} \tag{B.3}$$

where the st and sl subscripts indicate, respectively, whether the system is completely stuck throughout, or slips at any portion of, the entire fundamental period. Thus the Fourier Coefficients of the tangential force are similarly piecewise:

$$F_{Tc} = \begin{cases} F_{Tc,st} & k_T\,(X - \max(w)) < |\mu k_N y_0| \\ F_{Tc,sl} & k_T\,(X - \max(w)) \geq |\mu k_N y_0| \end{cases} \tag{B.4}$$

$$F_{Ts} = \begin{cases} F_{Ts,st} & k_T\,(X - \max(w)) < |\mu k_N y_0| \\ F_{Ts,sl} & k_T\,(X - \max(w)) \geq |\mu k_N y_0| \end{cases} \tag{B.5}$$

For response amplitudes where slip does not occur over the entire period (the trivial, linear case) $f_{T,st}(\theta) = k_T x$ and, when inserted for $f_T(\theta)$ in the integrations of Equations B.1 and B.2 yield the corresponding Fourier Coefficients:

$$F_{Tc,st} = 0 \tag{B.6}$$

$$F_{Ts,st} = k_T X \tag{B.7}$$

For amplitudes where slip does occur, $f_{T,sl}$ is piece-wise and the integrations of Equations B.1 and B.2 must be solved over five segments where the limits of integration are 0, 2π, and the instantaneous phase angles where the system transitions from slip to stick and vice-versa (vertical dashed lines in Fig. 4).

To find these limits of integration, the system is assumed to be at steady state so that the slider position is the same at the beginning and end of a cycle in x, or $w(0) = w(2\pi)$. Moreover, it can be shown that the stuck position of the slider is symmetric about zero. Thus, $w(t(\max(x)) = -w(t(\min(x)) = w_1$ is the slider position during slip. Therefore, the system first slips when $k_T(x(\theta_1) + w_1) = -\mu k_N y_0$ which can be used with Equation 36 to solve for θ_1, the instantaneous phase of the displacement where slip first occurs:

$$\theta_1 = \sin^{-1}\left(-\frac{w_1}{X} - \frac{\mu k_N y_0}{X k_T}\right) \tag{B.8}$$

Since x is assumed to be single-tone, the first reversal occurs at $\theta = \pi/2$. The slider position at transitions from slip to stick (w_1) is found by evaluating Equation 35 at $\theta = \pi/2$:

$$w_1 = X + \frac{\mu k_N y_0}{k_T} \tag{B.9}$$

To find $F_{Tc,sl}$ and $F_{Ts,sl}$ for response amplitudes that induce slip, the integrations of Equations B.1 and B.2 are evaluated over five segments of θ:

1. 0 to θ_1 (slider is stuck)
2. θ_1 to $\pi/2$ (slider is slipping)
3. $\pi/2$ to θ_3 (slider is stuck)
4. θ_3 to $3\pi/2$ (slider is slipping)
5. $3\pi/2$ to 2π (slider is stuck)

During the portions of the oscillation where the slider is stuck, $f_{T,sl}(\theta)$ is given by the first entry of Equation 34 while the second entry is used when the oscillator is slipping. This process yields the following expressions for the Fourier Coefficients of the tangential force of the Jenkins slider for amplitudes where slip occurs at some point throughout a period of oscillation:

$$F_{Tc,sl} = \frac{1}{\pi}\left(k_T X \sin^2\theta_1 + 2(k_T w_1 + \mu k_N y_0)\sin\theta_1 - k_T X + 2k_T w_1 - 2\mu k_N y_0\right) \tag{B.10}$$

$$F_{Ts,sl} = \frac{1}{\pi}\left(k_T X\left(\theta_1 + \frac{\pi}{2}\right) - 2k_T w_1\cos\theta_1 - 2\mu k_N y_0\cos\theta_1 - \frac{k_T X}{2}\sin 2\theta_1\right) \tag{B.11}$$

Authors' Contributions

Benjamin R Pacini conducted the harmonic balance analysis, performed analytical calculations, and wrote the journal. Robert J Kuether wrote and edited the journal and wrote algorithms for the harmonic balance computations. Deborah M Fowler wrote and edited the journal and wrote algorithms for the harmonic balance computations. Benjamin and Robert reviewed the submitted manuscript.

Acknowledgements

Sandia National Laboratories is a multimission laboratory managed and operated by National Technology & Engineering Solutions of Sandia, LLC, a wholly owned subsidiary of Honeywell International Inc., for the U.S. Department of Energy's National Nuclear Security Administration under contract DE-NA0003525.

This paper describes objective technical results and analysis. Any subjective views or opinions that might be expressed in the paper do not necessarily represent the views of the U.S. Department of Energy or the United States Government.

References

[1] P. Avitabile. *Modal testing: a practitioner's guide*. John Wiley Sons, 2018.

[2] D. J. Ewins. *Modal Testing: Theory, Practice, and Application*. John Wiley Sons, Bognor Regis, West Sussex, England, 2009.

[3] G. Kerschen, K. Worden, A. F. Vakakis, and J.-C. Golinval. Past, present and future of nonlinear system identification in structural dynamics. *Mechanical systems and signal processing*, 20(3):505–592, 2006.

[4] J.-P. Noël and G. Kerschen. Nonlinear system identification in structural dynamics: 10 more years of progress. *Mechanical Systems and Signal Processing*, 83:2–35, 2017.

[5] T. Al-Hababi, M. Cao, B. Saleh, N. F. Alkayem, and H. Xu. A critical review of nonlinear damping identification in structural dynamics: Methods, applications, and challenges. *Sensors*, 20(24), 2020.

[6] M. Jin, M. R. W. Brake, and H. Song. Comparison of nonlinear system identification methods for free decay measurements with application to jointed structures. *Journal of Sound and Vibration*, 453:268–293, 2019.

[7] M. Feldman. Non-linear system vibration analysis using hilbert transform—i. free vibration analysis method 'freevib'. *Mechanical Systems and Signal Processing*, 8(2):119–127, 1994.

[8] D. R. Roettgen and M. S. Allen. Nonlinear characterization of a bolted, industrial structure using a modal framework. *Mechanical Systems and Signal Processing*, 84:152–170, 2017.

[9] H. Sumali and R. A. Kellogg. Calculating damping from ring-down using hilbert transform and curve fitting. In *4th International Operational Modal Analysis Conference (IOMAC)*, Istanbul, Turkey, 2011.

[10] B. J. Moldenhauer. Nonlinear system identification methods for characterizing amplitude dependent modal properties. Doctor of philosophy dissertation, The University of Wisconsin-Madison, 2022.

[11] T. Karaağaçlı and H. N. Özgüven. Experimental modal analysis of nonlinear systems by using response-controlled stepped-sine testing. *Mechanical Systems and Signal Processing*, 146, 2021.

[12] T. Karaağaçlı and H. N. Özgüven. A frequency domain nonparametric identification method for nonlinear structures: Describing surface method. *Mechanical Systems and Signal Processing*, 144, 2020.

[13] M. Peeters, G. Kerschen, and J. Golinval. Dynamic testing of nonlinear vibrating structures using nonlinear normal modes. *Journal of Sound and Vibration*, 330:486–509, 2011.

[14] D. A. Ehrhardt and M. S. Allen. Measurement of nonlinear normal modes using multi-harmonic stepped force appropriation and free decay. *Mechanical Systems and Signal Processing*, 76-77:612–633, 2016.

[15] M. Scheel, S. Peter, R. I. Leine, and M. Krack. A phase resonance approach for modal testing of structures with nonlinear dissipation. *Journal of Sound and Vibration*, 135:56–73, 2018.

[16] S. Peter and R. I. Leine. Excitation power quantities in phase resonance testing of nonlinear systems with phase-locked-loop excitation. *Mechanical Systems and Signal Processing*, 96:139–158, 2017.

[17] V. Denis, M. Jossic, C. Giraud-Audine, B. Chomette, A. Renault, and O. Thomas. Identification of nonlinear modes using phase-locked-loop experimental continuation and normal form. *Mechanical Systems and Signal Processing*, 106:430–452, 2018.

[18] L. Renson, A. Gonzalez-Buelga, D. A. W. Barton, and S. A. Neild. Robust identification of backbone curves using control-based continuation. *Journal of Sound and Vibration*, 367:145–158, 2016.

[19] M. Volvert and G. Kerschen. Resonant phase lags of a duffing oscillator. *International Journal of Non-Linear Mechanics*, 146, 2022.

[20] M. Volvert and G. Kerschen. Phase resonance nonlinear modes of mechanical systems. *Journal of Sound and Vibration*, 511, 2021.

[21] M. Cenedese and G. Haller. How do conservative backbone curves perturb into forced responses? a melnikov function analysis. *Proceedings of the Royal Society A*, 476, 2020.

[22] M. Krack. Nonlinear modal analysis of nonconservative systems: Extension of the periodic motion concept. *Computers Structures*, 154:59–71, 2015.

[23] T. L. Hill, A. Cammarano, S. A. Neild, and D. J. Wagg. Interpreting the forced responses of a two-degree-of-freedom nonlinear oscillator using backbone curves. *Journal of Sound and Vibration*, 349:276–288, 2015.

[24] R. J. Kuether, L. Renson, T. Detroux, C. Grappasonni, G. Kerschen, and M. S. Allen. Nonlinear normal modes, modal interactions and isolated resonance curves. *Journal of Sound and Vibration*, 351:299–310, 2015.

[25] Y. Sun, A. Vizzaccaro, J. Yuan, and L. Salles. An extended energy balance method for resonance prediction in forced response of systems with non-conservative nonlinearities using damped nonlinear normal mode. *Nonlinear Dynamics*, 103: 3315–3333, 2021.

[26] R. M. Lacayo and M. S. Allen. Updating structural models containing nonlinear iwan joints using quasi-static modal analysis. *Mechanical systems and signal processing*, 118:133–157, 2019.

[27] A. Carrella and D. J. Ewins. Identifying and quantifying structural nonlinearities in engineering applications from measured frequency response functions. *Mechanical Systems and Signal Processing*, 25(3):1011–1027, 2011.

[28] D. M. Fowler, R. J. Kuether, and B. R. Pacini. Multi-input, multi-harmonic nonlinear phase resonance simulations with harmonic balance. Report, U.S. Department of Energy OSTI, 2021.

[29] N. Mork, J. Shedleski, J. Cosner, D. Fowler, B. R. Pacini, R. J. Kuether, and D. R. Roettgen. Optimizing test setup parameters for force appropriation testing. In *41st International Modal Analysis Conference (IMAC XLI)*, Austin, TX, USA, 2023.

[30] B. R. Pacini, R. J. Kuether, and D. R. Roettgen. Shaker-structure interaction modeling and analysis for nonlinear force appropriation testing. *Mechanical Systems and Signal Processing*, 162, 2022.

[31] C. Siewert, L. Panning, J. Wallaschek, and C. Richter. Multiharmonic forced response analysis of a turbine blading coupled by nonlinear contact forces. *Journal of Engineering for Gas Turbines and Power*, 132(8), 2010.

[32] S. Zucca and C. M. Firrone. Nonlinear dynamics of mechanical systems with friction contacts: Coupled static and dynamic multi-harmonic balance method and multiple solutions. *Journal of Sound and Vibration*, 333(3):916–926, 2014.

[33] R. Seydel. *Practical bifurcation and stability analysis*, volume 5. Springer Science Business Media, 2009.

[34] B. J. Deaner, M. S. Allen, M. J. Starr, and D. J. Segalman. Application of viscous and iwan modal damping models to experimental measurements from bolted structures. *Journal of Vibration and Acoustics*, 137(2), 2015.

[35] R. L. Mayes, B. R. Pacini, and D. R. Roettgen. A modal model to simulate typical structural dynamic nonlinearity. In *Dynamics of Coupled Structures, Volume 4: Proceedings of the 34th IMAC, A Conference and Exposition on Structural Dynamics*. Springer International Publishing, 2016.

[36] M. Debeurre, S. Benacchio, A. Grolet, C. Grenat, C. Giraud-Audine, and O. Thomas. Phase resonance testing of highly flexible structures: Measurement of conservative nonlinear modes and nonlinear damping identification. *Mechanical Systems and Signal Processing*, 215, 2024.

[37] H. Baruh. *Analytical Dynamics*. WCB/The McGraw-Hill Companies, Inc, 1999.

[38] B. R. Pacini and D. R. Roettgen. Practical considerations for force appropriation testing of a bolted structure. In *Proceedings of the 38th International Modal Analysis Conference*, 2020.

[39] K. Worden and G. R. Tomlinson. *Nonlinearity in Structural Dynamics*, pages 81–101. Institute of Physics Publishing, Bristol, UK, 2001.

[40] J. H. Griffin. Friction damping of resonant stresses in gas turbine engine airfoils. *Journal of engineering for power*, 102(2): 329–333, 1980.

[41] L. Woiwode, A. F. Vakakis, and M. Krack. Analysis of the non-periodic oscillations of a self-excited friction-damped system with closely spaced modes. *Nonlinear Dynamics*, 106:1659–1673, 2021.